Andreia Filipa Garcia de Carvalho
Bachelor of Science in Materials Engineering

Comprehend the Optical, Morphological, and Electrical Characteristic of Air Processed Polymer Solar Cells

Dissertation to obtain the Master Degree
in
Materials Engineering

Supervisor: Dr. Vishal Bharti, Post Doctoral Researcher
Departamento de Ciência dos Materiais, Faculdade de Ciências e Tecnologia-Universidade Nova de Lisboa, Caparica, Portugal

Co-Supervisor: Dra. Isabel Maria das Mercês Ferreira, Associate Professor
Departamento de Ciência dos Materiais, Faculdade de Ciências e Tecnologia-Universidade Nova de Lisboa, Caparica, Portugal

Jury:
President: Dr. Alexandre Velhinho
Examiner: Dr. Vishal Sharma
Member: Dr. Vishal Bharti

FACULDADE DE
CIÊNCIAS E TECNOLOGIA
UNIVERSIDADE NOVA DE LISBOA

December, 2020

Comprehend the Optical, Morphological, and Electrical Characteristic of Air Processed Polymer Solar Cells

Para os meus avós, Tereza e Victor.

Acknowledgement

In the first place, I would like to thank my extraordinary supervisor, Dr Vishal Bharti, for all the help, patience, training, guidance and encouragement. It has been a great privilege and honour to share the laboratory with you and develop this dissertation. Thank you for sharing your knowledge and wisdom with me. I am grateful and proud to say that I have learnt from the best.

Em segundo lugar, gostaria de agradecer à minha co-orientadora, Prof. Drª Isabel Ferreira, pela honrosa oportunidade de desenvolver este tema. Muitíssimo obrigada pela confiança depositada, pelo apoio nos momentos mais críticos e pelo conhecimento transmitido, quer durante esta dissertação, quer durante estes cinco anos. Gostaria também de agradecer aos membros da sua equipa, nomeadamente, à Drª. Ana Marques, por todas as medições de AFM e esclarecimentos de dúvidas; ao David Sousa pelas caracterizações de PL e pela sua boa disposição e à Catarina Bianchi por me fornecer todo o ITO, bem como por todas as dúvidas esclarecidas.

Não posso também deixar de agradecer a toda a equipa do DCM pela ajuda e apoio prestado no decorrer desta dissertação e durante estes cinco anos.

Um obrigada especial a todos os meu amigos que me acompanharam durante todo o percurso. Sinto-me grata. Quero agradecer à minha amiga Beatriz, uma verdadeira e fiel companheira. Obrigada pela tua amizade e por ter tido o privilégio de partilhar contigo a descoberta dos encantos polacos. Guardo-os para sempre no meu coração. Não posso também deixar de agradecer ao meu grande amigo Bernardo pela sua amizade, companheirismo e paciência. Um obrigada muito especial às minhas amigas, Madalena e Inês, pela vossa amizade e por todas as nossas aventuras. Quero tambem agradecer à minha afilhada, Margarida, pelo apoio, sorrisos, gargalhadas e carinho. Ao meu amigo Mendonça pelo nosso excelente trabalho em parceria. E obrigada às minhas amigas de longa data: Diana; Larisa e Débora. Agradeço a todos estes e a todos os que não estão aqui mencionados. Obrigada por terem feito parte deste percurso e que caminhemos juntos no próximo.

Finalmente, gostaria de agradecer à minha família, que tanto amo. Um Obrigada aos meus pais, pelo apoio e amor incondicional. Mesmo estado longe fizeram sempre os possíveis para acompanharem o meu percurso, que nem sempre foi fácil. Valorizo todos os vossos sacrifícios. São um exemplo de amor, força e superação. Um obrigada aos meus avós, Tereza e Victor, pelo apoio e força que me deram durante toda esta “luta”. Por todas as palavras de conforto e abraços tão especiais. Obrigada à minha avó Mariana, uma pessoa pequenin, mas que ocupa um espaço muito grande no meu coração. Um obrigada à minha tia Zulmira e ao meu tio Zé António pela amizade e preocupação. E por último mas não menos importante, Obrigada ao meu namorado, João, pelo amor, paciência, apoio e carinho. Obrigada por seres o meu chão.

Obrigada a todos os que fizeram parte desta pequena mas intensa viagem.

Abstract

Solar energy via photovoltaic (PV) is a promising and freely accessible energy source that has become the main route for managing long term challenges in the energy crisis. Organic solar cells (OSCs) have raised interest in the scientific community due to their enormous potential in solar industry such as mechanical flexibility, exceptional processability, and capability of large-area roll-to-roll (R2R) manufacturing.

In this work, we emphasize to understand the correlation between optical (absorbance and photoluminescence) and morphology properties of air processed photoactive layer, which are prepared at different spin-speeds (800 rpm, 1000 rpm, 1200 rpm, and 1500 rpm) and $PC_{61}BM$ concentration (1.0:0.6, 1.0:0.8 and 1.0:1.0 ratios) and its influence on the performance of OSCs devices. Here, OSCs devices have been fabricated in an inverted bulk heterojunction (BHJ) device configuration viz. sputtered Indium Thin Oxide (sITO)/Zinc oxide (ZnO)/P3HT:$PC_{61}BM$/ Molybdenum trioxide (MoO_3)/Silver (Ag). The sITO, ZnO, MoO_3, and Ag were introduced as a transparent cathode electrode, electron transport layer (ETL), hole transport layer (HTL), and an anode electrode, respectively. The blend of regioregular poly(3-hexylthiophene-2,5-diyl) (rrP3HT), donor polymer, and [6,6] phenylC61-butyric acid methyl ester ($PC_{61}BM$), acceptor molecule, is employed as a photoactive layer in the proposed devices. All the samples (for optical and morphological measurements) and solar cell devices were prepared via spin-coating technique without controlling the atmospheric conditions. A thin interface layer of MoO_3 (10 nm, 0.2-0.5 Å/sec) and anode electrode (Ag, ≈ 150 nm, 1.5 Å/sec) were both deposited, sequentially, on the photoactive layer using thermal evaporation with a vacuum of 10^{-6} Torr. The photovoltaic performance parameters were explored by using current-voltage (*J-V*) characteristics.

Furthermore, electrochemical impedance spectroscopy (EIS) was used to generate an electrical model for the extraction of charge transport parameters of air processed OSCs devices such as the chemical capacitance ($C\mu$), effective lifetime (τ_n), diffusion time (τ_d) and charge carrier mobility (μ). Additionally, the long-term stability of the produced photovoltaic devices is reported.

Keywords: Organic solar cells, P3HT:$PC_{61}BM$, Open-air fabrication, spin-coating technique, Absorption, Morphology, Impedance Measurement

Resumo

A energia solar fotovoltaica é uma fonte promissora e acessível de energia que se tornou a rota principal para a gestão dos desafios impostos pela crise energética a longo termo. As Células Solares Orgânicas (CSOs) captaram o interesse da comunidade científica devido ao seu enorme potencial industrial como a sua flexibilidade mecânica, o processamento exceptcional e a capacidade de produção *roll-to-roll* (R2R) a larga escala.

Neste trabalho, deu-se ênfase à correlação entre as propriedades óticas (absorbância e fotoluminescência) e morfológicas das camadas activas processadas em atmosfera aberta, as quias preparadas a diferentes *spin-speeds* (800rpm, 1200rpm, 1500rpm), possuem diferentes concentrações de $PC_{61}BM$ (a 1.0:0.6, 1.0:0.8 e 1.0:1.0 proporções) e a sua influência na performance das CSOs.

Aqui, as CSOs foram fabricadas numa configuração de dispositivo invertida baseda no principio de heterojunção (BHJ). O Óxido de Indio Estanho (ITO), preparado pela técnica *Sputtering* RF, sITO/Óxido de Zinco (ZnO)/P3HT:$PC_{61}BM$/ Tróxido de molibdénio (MoO_3)/Prata (Ag). sITO, ZnO, MoO_3, e Ag foram introduzidos como cátodo (electrodo) transparente, camada transportadora de eletrões (ETL), camada de transportadora de buracos (HTL) e ânodo (electrodo), respetivamente. A mistura de regioregular poli (3-hexiltiofeno) (rrP3HT), polímero doador, e [6,6]-fenil-C_{61}-ácido butírivo-metil ester ($PC_{61}BM$), a molécula aceitadora, foi utilizada como camada ativa nos dispositivos propostos. Todas as amostras (para as avaliações óticas e morfológicas) e as células solares foram preparadas através da técnica de *spin-coating* , sem controlo das condições atmosféricas. Uma interface fina de MoO_3 (10 nm, 0.2-0.5 Å/sec) e um ânodo (elétrodo) (Ag, ≈ 150 nm, 1.5 Å/sec) foram ambos depositados, sequencialmente, na camada activa através da sua evaporação térmica a vácuo de 10^{-6} Torr. Os parâmetros de performance fotovoltaica foram explorados através das curvas caracteristicas *J-V*.

Além disso, a espectroscopia de impedância eletroquímica (EIS) foi utilizada para gerar um modelo elétrico para a extracção dos parâmetros de transporte de carga de dispositivos solares processados em atmosfera aberta, tais como capacitância química ($C\mu$), tempo de vida efetivo (τ_n), tempo de difusão (τ_d) e mobilidade global (μ). Adicionalmente a estabilidade de longo-termo das células produzidas é reportada.

Palavra-Chave: Células Solares Orgâncias, P3HT:$PC_{61}BM$, atmosfera aberta, *spin-coating*, Absorção, Morfologia, Impedâncias

Abbreviation

PV	Photovoltaic	**PCE**	Power conversion efficiency
OSCs	Organic Solar Cells	**Voc**	Open circuit voltage
SCs	Solar Cells	**Isc**	Short circuit current
OPV	Organic Photovoltaic	**Jsc**	Short circuit current density
BHJ	Bulk-heterojunction	**Pmax**	Maximum power
sITO	Sputtered Indium Tin Oxide	$\mathbf{I_{MP}}$	Current at maximum power
rrP3HT	Regioregular poly(3-hexylthiophene-2,5-diyl)	$\mathbf{V_{MP}}$	Voltage at maximum power
PC$_{61}$BM	[6,6] phenylC61-butyric acid methyl ester	**Pin**	Incident Light
DCB	Dichlorobenzene	**FF**	Fill Factor
ETL	Electron Transport Layer	$\mathbf{R_S}$	Series resistance
HTL	Hole Transport Layer	$\mathbf{R_{SH}}$	Shunt resistance
HTM	Hole Transport Material	**EIS**	Electrochemical Impedance Spectroscopy
ETM	Electron Transport Materials	**AC**	Alternate current
LUMO	Lowest Unoccupied Molecular Orbital	**CPE**	Constant phase element
HOMO	Highest Occupied Molecular Orbital	$\mathbf{C\mu}$	Chemical capacitance
DSSCs	Dye-Sensitized Solar Cells	$\boldsymbol{\tau_n}$	Effective lifetime
Poly-Si	Polycrystalline Silicon	$\boldsymbol{\tau_d}$	Diffusion lifetime
PTFE	Polytetrafluoroethylene	$\boldsymbol{\mu}$	Charge carrier mobility
NPs	Nanoparticles	$\mathbf{R_t}$	Transport resistance
UV-visible	Ultraviolet (UV)-visible	$\mathbf{R_{rec}}$	Recombination resistance
PL	Photoluminescence	$\mathbf{k_B}$	Boltzmann constant
AFM	Atomic Force Microscopy	**T**	Temperature
TM	Tapping mode	**L**	Thickness
I-V	Current-Voltage	**CAS**	Chemical Abstract Service

Symbols

Ag	Silver
Au	Gold
Cu	Copper
KOH	Potassium Hidroxide
TiO_2	Titanium Dioxide
MoO_3	Molybdenum Trioxide
ZnO	Zinc oxide
$Zn(OAc)_2$	Zinc Acetate Dihydrate
µL	Microliter
mL	Millilitre
mg	Miligrame
cm^2	Square Centimeters
mm^3	Cubic Millimeter
nm -	Nanometer
µm	Micrometre
Å	Ångström
mA/cm^2	Milliamperes per Square Centimeter
Hz	Hertz
hr	Hour
min	Minute
N/m	Newton metre
W	Watt
°C	Degrees Celsius
mBar	milibar
%	Percentage
rpm	Rotations per minute
sec	Seconds
V	Voltage
mV	Millivolt
λ	Wavelength
Ω	Ohms
Ω/cm^2	Ohms Per Cemitmeter Square
$cm^2V^{-1}s^{-1}$	Centimetre Square per Voltage vs Seconds

List of Contents

List of Figures

List of Tables

Motivation and Objectives

The World's energy demand is growing at a break-neck speed due to the population explosion and technological advancements. Solar energy is a promising and freely accessible energy source for managing long term challenges in the energy crisis. [1]Polycrystalline silicon (poly-Si) solar cells (SCs) are currently the most popular photovoltaic technology for industrial purposes due to their high efficiencies above 20%. [2]Despite all the advantages, there are inherent disadvantages such as high cost of critical processing techniques as it requires high temperature or vacuum. The main competition of silicon photovoltaic technology comes from a variety of thin-film solar cells, which involve simple deposition methods, low-cost production without compromising the quality of the semiconductor. [3]Solution-processed organic solar cells (OSCs) have raised interest in the scientific community due to their enormous potential in the solar industry as a consequence of their attractive characteristics. Moreover, OSCs are promising as a renewable energy source due to low resource extraction and no emission of greenhouse gases during use. [4]

In 1986, W. C. Tang reported the first bilayer OSCs successfully with an efficiency of 1%. [5]A few years later, Alan Heeger observed an ultrafast photoinduced electron transfer leading to the enhancement in charge photogeneration yield.[6]The concept of heterojunction, born with the first dye-dispersed/BHJ produced by Masahiro Hiramoto in 1991, which has since been widely exploited in several donor/ acceptor (D/A) cells. In the past few years, different strategies have been employed to control the morphology and further improve efficiency. [7]Currently, the PCE record of an OSCs is 18.22% (certified 17.6%), based on D18:Y6, with an effective area of 0.026 cm^2. [8]It is intended to improve the efficiency and lifetime of OSCs to push them to the marketplace within a few years. However, all of this manufacturing was conducted inside the glovebox. Only a small percentage attempted to develop the fabrication in an open-air atmosphere. [9], [10]

The new materials such as low bandgap polymers and non-fullerene acceptors available in the market are so expensive in comparison to the well-studied system rrP3HT donor polymer and fullerene derivative $PC_{61}BM$ acceptor. Most PCE values have been found as being 3% and 4% by applying an inverted geometry, which has attracted much attention because of their air-stability. [11]This type of architecture allows the use of a high work function metal contact, and a low work function metal oxide as an electron transporting layer (ETL) to modify the ITO substrate, offering a better ambient surface to the device. [12]

In this research work, we have fabricated all the devices based on the blend of rrP3HT:$P_{61}BM$ in the inverted device configuration viz. sITO/ZnO/rrP3HT:$PC_{61}BM$/MoO_3/Ag. All the devices are fabricated in an ambient environment without controlling the temperature and humidity (without using the glove box), which reduced my overall research costs to some extent. The main objective of this research work is:

1. Optical (absorbance and photoluminesce), morphological and electrical characterization of the OSCs processed in open-air by varying the spin-speed (800 rpm, 1000 rpm, 1200 rpm and 1500 rpm) and $PC_{61}BM$ concentration (1.0:0.6, 1.0:0.8 and 1.0:1.0). Subsequent properties correlation;

2. Design an electrical model for air processed $P3HT:PC_{61}BM$ based organic solar cell devices by using Impedance spectroscopy. This model will help to evaluate the charge transport parameter like transport resistance (R_t), recombination resistance (R_{rec}), effective lifetime (τ_n), diffusion time (τ_d) and electron mobility (μ_n) of the charge carrier within the OSCs devices. The electrical model will be applicable for air processed $rrP3HT:PC_{61}BM$ with any thickness or acceptor concentration.

Chapter 1: Introduction

A brief introduction to the organic semiconductor and organic solar cells is presented in this chapter, as it is required to comprehend the results discussed in this research work.

Nowadays, more than 80% of the world's energy mix is derived from fossil fuels, which contributes to the gradual increase of CO_2 in the atmosphere. [13]As a result of this considerable increase, today's photosynthetic organisms are unable to absorb this huge amount of extra CO_2 leading to a rise of both temperature and global sea levels, which are likely to have more devasting effects for humans and other existing life forms on Earth. [14]Therefore, given the urgent need for energy security and climate change mitigation, solar cells have gained wide attention in the last decade, emerging as a feasible feature to sustainable energy manner. SCs can convert the radiation provided by the sun into electric energy based on the photovoltaic effect. [3]

This powerful technology is divided into three generations according to their stages of development: the first generation SCs are based on crystalline Si (c-Si); the second-generation SCs are based on thin-film technology, which has frequently encompass vapour deposited semiconductors; and the third-generation SCs can be assessed in a few different subjects such as dye-sensitized solar cells (DSSCs), polymers and small molecules-based cells, and as a result of the mixture of organic and inorganic materials hybrid solar cells emerged. [1], [2]

Organic solar cells (OSCs), third-generation SCs and ground-breaking technology are based on thin film organic semiconducting polymers. These materials enable the fabrication of solar cells with several potential advantages, such as lightweight, flexibility, low-cost manufacturing, as well as large-area feasibility. Furthermore, the semiconducting polymers combine outstanding properties of optoelectronic and mechanical, even processing, of conventional semiconductors (e.g. metals) and polymer materials. [15]However, OSCs exhibit low photocurrent generation, low power conversion efficiency (PCE), depending on the cell structure, and long-term stability.

1.1 Organic Semiconductors

The broad field of organic electronics includes the utilization of conductive conjugated polymers (10-100kDA) or π -bonded molecules in electronic applications such as photovoltaic devices. Organic semiconductors are carbon-based macromolecules characterized by intense and relatively week intramolecular and intermolecular electronic interactions, respectively, which creates a quasi-dimensional system.[16] As a consequence of a quasi-dimensional system of organic materials, an exclusive properties combination typical of plastics (mechanical strength, adjustable physicochemical properties and solubility) and electrical conductivities typical of metals are achieved. The conduction in an organic semiconductor arises from the presence of π -conjugation in carbon chains of conjugated polymers with alternating single and double bonds (Figure 1).

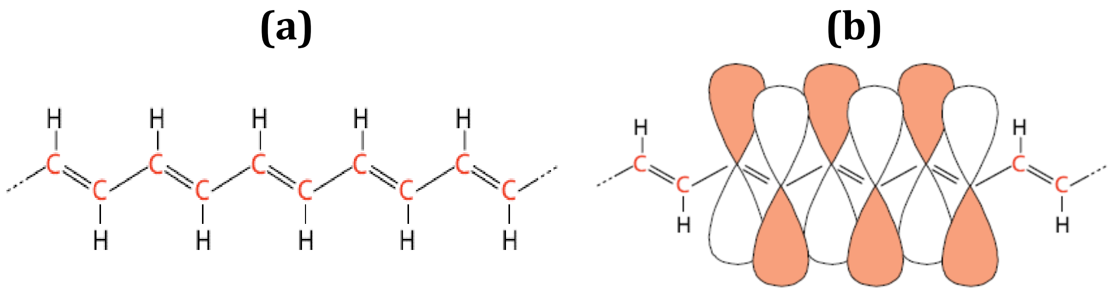

Figure 1 | Organic semiconductor (a) Conjugated polymer: part of a polyacetylene chain containing alternating single and double bonds. (b) π -bonds between overlapping *pz-orbitals* with adjacent orbitals are in an anti-bonding configuration. [17]

1.2 Classification of OSCs

In electronics application, an organic semiconductor layer is placed between the two electrodes with different work functions. The difference in the work function of electrodes creates an electric field which provides the driving energy to the charge carriers within the organic layer under different conditions. Initially, the organic solar cells are classified, into three different types, depending on the composition of the photoactive layer. In this section, we present an overview of the historical modifications in organic solar cells.

1.2.1 Single layer OCSs: In an earlier phase of organic solar cells, the devices were fabricated by placing a single organic semiconductor layer between two metal electrodes (Figure 2a). [18]This structure provides only two interfaces at which photo excitons can dissociate. In this type of device, the charge carrier extraction was achieved with the help of an electric field generated at the interface which limits the efficient exciton dissociation. The reported power conversion efficiency (PCE) of these OSCs (around 0.1%) was very low because of short diffusion length and poor charge carrier mobility of the organic semiconductor materials (10^{-3} cm^2/V·s). [19]

1.2.2 Bilayer OSCs: In a bilayer OSCs, the donor (p-type)and acceptor (n-type) materials were stacked sequentially and placed in between two electrodes (Figure 2b). In 1986, C. W. Tang proposed a bi-layer structure, using phthalocyanines as a donor and perylene derivatives as an acceptor layer with an efficiency of 1%. [5]In this structure, the exciton dissociation occurs at the interface of donor and acceptor layer, with the help of orbital energy offsets between both unoccupied molecular orbitals (LUMOs). [20]The PCE of bilayer OSCs is still restrained by a low charges generation, mainly due to the low exciton diffusion length in the donor and acceptor phases (10-15 nm) and insufficient D/A heterojunction interfacial area for excitons dissociation. [21],[22]

1.2.3 Bulk-Heterojunction OSCs*:* In 1995, Yu et al. first reported bulk-heterojunction (BHJ) solar cells (Figure 2c) with a blending of conjugated polymer (donor) and fullerene (acceptor) as the active materials, from which resulted an interpenetrating network with large interface areas.

[23],[24]This junction represents the most promising device structure for high-efficiency organic solar cells. The main reason is due to the creation of a bicontinuous phase separation network, which enhances the exciton dissociation and charges transport. Therefore, the BHJ is capable of overcoming the small exciton diffusion length limitation, unlike other structures (e.g. single layer and bilayer OSCs.)

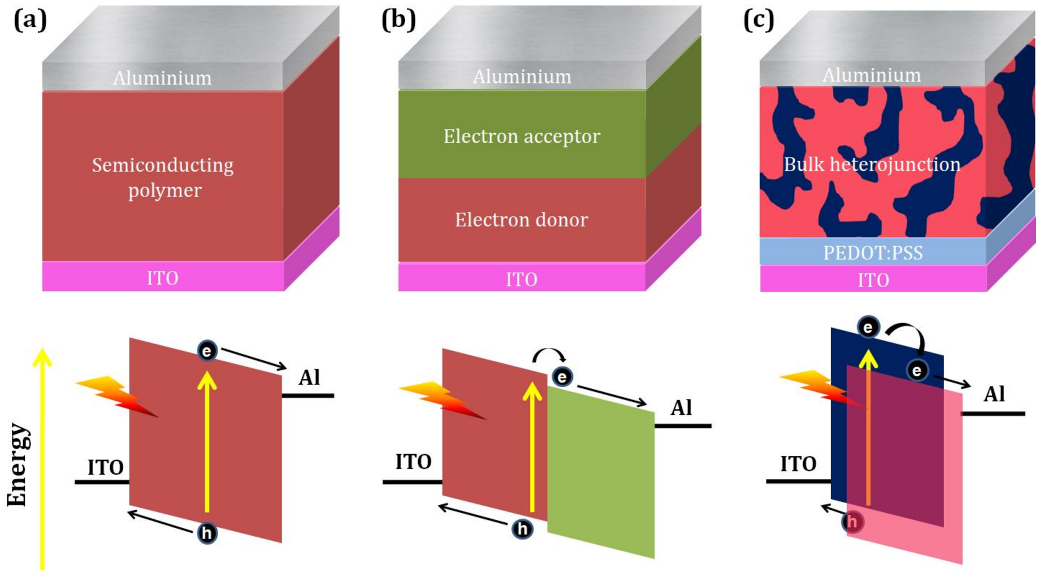

Figure 2 | Classification of OSCs (a) Single layer (b) Bi-layer (c) Bulk-heterojunction.

1.3 Working Mechanism of Bulk-heterojunction OSCs

The photoactive layer of a bulk heterojunction OSCs is consisted of donor and acceptor molecules. As donors usually conjugated polymers (P3HT) are used and as acceptors fullerene derivatives (PCBM). These materials are classified as organic semiconductors with their high absorption coefficient and electrical conductivity. A schematic diagram of the energy levels of a typical donor-acceptor system is shown in Figure 3(a). In a state of the art process, the conjugated polymers (donor) are responsible for the generation of a bound electron-hole pair (exciton) with photon absorption having energy greater than the bandgap of the active layer. [20], [25],[26]

1.3.1 Light Absorption and Exciton Generation: When the light (photons) interacts within the bulk-heterojunction photoactive layer, the π-electrons of conjugated polymers can be excited by absorbing a photon. This corresponds to the first optical excitation from the highest occupied molecular orbital (HOMO) to the lowest unoccupied molecular orbital (LUMO). As a result, a Frenkel exciton is generated within the interpenetrating network of donor and acceptor blend. [16], [27]

1.3.2 Exciton Diffusion: The Frenkel excitons generated via light absorption start to transport towards the interface through the diffusion mechanism. The diffusion length of an exciton is a vital property of the conjugated polymers that varies from 10-20 nm. [28]The diffusion length of an exciton within organic materials is inversely proportional to exciton lifetime. [29]Therefore, the thickness of the photoactive layer (Donor: Acceptor) is restricted by the exciton diffusion length. The exciton generated away from diffusion length undergoes geminate recombination. [30]

1.3.3 Exciton Dissociation: This diffusion mechanism of the exciton is followed by a dissociation mechanism for those excitons that are close enough to the donor-acceptor interface. At the donor-acceptor interface, the energy band offsets between donor and acceptor LUMO levels help to dissociate the exciton into a free charge carrier. The free electrons move towards the acceptor side, and the hole remains in the donor side. During this process, some of the excitons undergo trap assisted recombination. [16], [26], [31]

1.3.4 Charge Collection: After dissociation, the free charge carriers move towards the respective electrodes with the help of a field generated by electron and transport layers. In organic solar cells, during this process, some of the charge carriers undergo bimolecular recombination. The collected charge carriers help to generate photocurrent. [32]

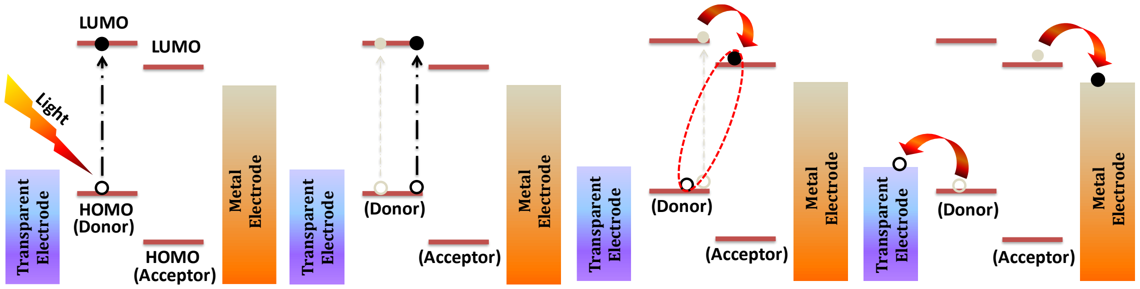

(a) Light absorption and exciton generation **(b) Exciton diffusion** **(c) Exciton dissociation** **(d) Charge collection**

Figure 3 | Schematic of the working principles of an organic solar cell (1) Light absorption and Exciton generation, (2) Exciton diffusion, (3) Exciton dissociation, (4) Collection of charges at the electrodes.

1.4 Different Configuration in Bulk-heterojunction OSCs

The bulk-heterojunction OSCs usually consists of an electron or hole interface layer on top of an indium tin oxide (ITO) conductive glass followed by a photoactive layer (blend of donor and acceptor), a hole or electron interface layer, and top metal electrode (Al, Ag). The nature and order of the interfacial layers and the nature of the metal electrode define the configuration of OSCs. [33]

1.4.1 Conventional Configuration: In this configuration, after the exciton dissociation, the holes are extracted towards ITO electrode through-hole transport layer (PEDOT:PSS, MoO_3) and the electrons are extracted towards the top metal electrode by an electron transport layer (ZnO, PFN). In this case, the ITO electrode behaves as an Anode and the top metal electrode acts as a cathode. [34], [35]

1.4.2 Inverted Configuration: In this configuration, after the exciton dissociation, the electrons are extracted towards ITO electrode through electron transport layer (ZnO, PFN) and the hole is extracted towards the top metal electrode by a hole transport layer (PEDOT:PSS, MoO_3). In this case, the ITO electrode behaves as a cathode and the top metal electrode acts as an anode. [12], [36]

1.4.3 Role of interface layer: The interface layer (ETL and HTL) used between electrodes and the photoactive layer play an important role in the efficiency enhancement and stability of the OSCs devices. [37]In general, these interface layers fulfil several requirements, like establishing an ohmic contact between the photoactive layer and the electrodes, act as a blocking layer for confining electron or hole transport to their respective electrode, obstruct the reaction (chemical or physical) between the photoactive layer and electrodes, and some interface layer (ZnO) absorbs the UV light and protects the photoactive layer from UV light degradation. [36], [38], [39]

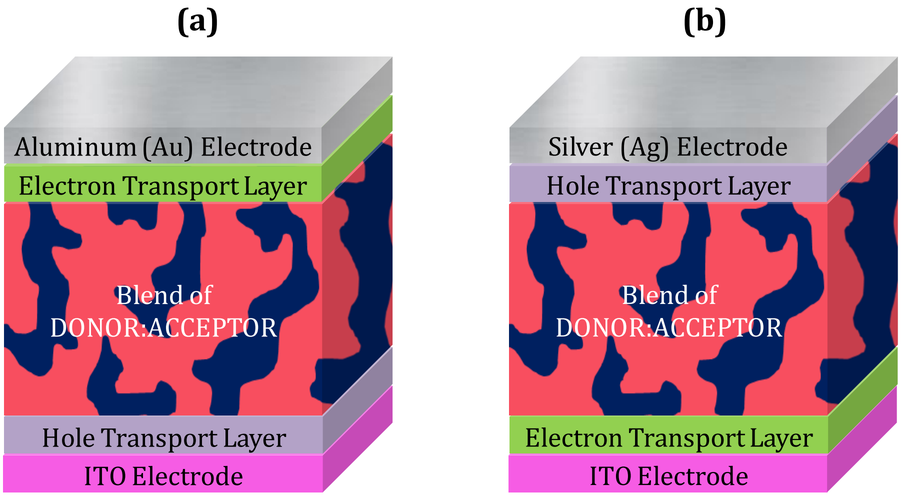

Figure 4 | Device configuration of Bulk-Heterojunction OSCs (a) Conventional (b) Inverted.

1.5 Fabrication Techniques for OSCs

In comparison with the present photovoltaic technologies (Silicon photovoltaic), OSCs is well recognized as a low-cost processing technology due to its solution processability. The main feature of the solution-processing technique is that OSCs could be fabricated at ambient pressure and ambient temperature, reducing the manufacturing costs. The fabrication of OSCs is broadly divided into two parts i.e. coating and printing, which are suitable from the lab scale up to large scale production. [15], [40]

1.5.1 Drop Casting: The drop casting is one of the simplest approaches for the deposition of a thin film without requiring any specific equipment. [41] In this method, the desired solution is dispensed on the substrate and allowed to cause the evaporation of the solvent. However, in this technique, it is very difficult to control the uniformity and thickness of the applied layer. The other variables that affect the film formation are solution concentration, substrate wettability, the rate of evaporation of the solvent, and the drying process of the film. [41],[42]

1.5.2 Spin Casting: It is the most extensively used coating technique for the fabrication of OSCs on a laboratory-scale. [43]In this method, the substrate is placed on the rotary chunk and the solution is dispensed on the substrate. The spinning of the chunk generates a centrifugal force which shears the unwanted solution, spreads the solution uniformly and dries the film simultaneously. [44]Here, the thickness of the deposited film is controlled by the spin rate of the chunk and rotation time. The spin casting provides homogeneous films with high reproducibility in thickness and morphology. The main limitations of this technique are wastage of the desired solution (a large amount of solution is ejected at the start of the spinning) and only effective for the film coating on small substrates. [45]

1.5.3 Spray Coating: The spray coating method is based on the deposition of sub-micrometric droplets on the substrate ejected by using a jet stream or airflow. The aerosol is created by passing solution ink through a nozzle supported by air pressure. The handling of the nozzle over the substrate is optimized to ensure that the coating is spread uniformly to the substrate.[46], [47]In general, the spray coating is divided into two ways of processing i.e. Airbrush spray and Ultrasonic spray. In comparison to spin coating, this technique can be used to coat a large substrate. [48]

1.5.4 Slot-die Coating: In this method, the solution ink is pump through a coating head which should be placed close to the moving substrate. The solution ink flows through the head at a selected rate and the substrate is moved underneath with determined speed. This method is a one-dimensional coating approach, allowing to depose layers of materials with a well-defined thickness. [49]The utilization of an exact amount of solution ink could be a deposit on the substrate, reducing the material wastage. The main feature of this technique is that it is scalable i.e this process can be used in roll-to-roll processing technique for large scale production. [50]The main drawback of this technique is that it is more expensive for primary research and development. [51]

1.6 Background and motivation

Solution-processed polymer solar cells (PSCs) is a promising photovoltaic technology due to its several advantages such as lightweight, flexibility and possibility for large-volume manufacture while using low-cost materials. In 1995, Heeger A.J. et al. reported the first well-know bulk heterojunction (BHJ) polymer-fullerene solar cells which are used until today. [6]Nowadays, the most extensively studied polymer-fullerene system is based on the blend of poly(3- hexyl thiophene) and [6,6]-phenyl-C61-butyric acid methyl ester (P3HT:$PC_{61}BM$) with certified power conversion efficiencies (PCEs) reported of 4.5% to 6%. [2], [52]However, all of these studies are conducted on devices fabricated under a glove box, which makes their fabrication highly complicated, expensive and fitted only to laboratory scale.

Therefore, facing this lack of knowledge on how the open-air fabrication affects the device performance, this study is justified and raises awareness on this subject. To this end, the objective of this research is to fabricate and analyze the air processed PSCs in an inverted BHJ configuration viz. sITO/ZnO/rrP3HT:$PC_{61}BM/MoO_3$/Ag. It is intended to understand the correlation between optical and morphology properties of air processed photoactive layer, prepared at different spin-speeds (800 rpm, 1000 rpm, 1200 rpm and 1500 rpm) and $PC_{61}BM$ concentrations (1.0:0.6, 1.0:0.8 and 1.0:1.0) and its influence on the performance of the proposed PSCs devices. Furthermore, electrochemical impedance spectroscopy (EIS) is used to design an electrical model to understand the charge transport mechanism in air processed PSCs. In this way, understanding the underlying optical, morphological, electrical and device stability/lifetime is a pivotal advance in PSCs towards commercialization, enhancing the energy transition. *In this work, we have used the Spin Coating method for the deposition of films and the fabrication of OSCs devices.*

Chapter 2: Experimental Methodology

This chapter provides a general overview of materials, fabrication process of OSCs and characterization & measurement techniques used in this research work. The materials used in this work are either purchased from the company or synthesized and prepared by me with the help of group members.

2.1 Transparent Conductive Electrode (TCO): In this work, we have used self sputtered indium tin oxide (sITO) electrode. The sITO (1.50×10^2 Ωcm^{-1}) were deposited by an RF magnetron Sputtering from MANTIS DEPOSITION LDT (Figure A7(a) in Appendix A) using an ITO target (In_2O_3:SnO_2 90:10) supplied by Super Conductor Materials Inc., for 60 min at 50W and a working pressure between 2.7-3.4 mbar.

2.2 Synthesis of ZnO nanoparticles: The ZnO nanoparticles, used as an electron transport layer in OSCs devices, were synthesized via hydroxylation, of Zinc acetate dihydrate ($Zn(OAc)_2$) with potassium hydroxide (KOH) in the Methanol (MeOH) solvent. [53]The description of the synthesis process is illustrated in section A.2 of Appendix A.

2.3 Fabrication of OSCs: The OSCs proposed in this work are fabricated in an inverted device configuration viz. sITO/ZnO/P3HT:$PC_{61}BM$/MoO_3/Ag. These devices were prepared at different rpm speed (800, 1000, 1200, and 1500 rpm) and at different blend ratio of P3HT: $PC_{61}BM$ (1.0:0.6, 1.0:0.8, and 1.0:1.0). The fabrication process of OSCs devices goes as follows:

2.3.1 Etching of sITO: In the first step, sITO coated glass substrates (100 x 100 x 1.10 mm^3) were carefully cut into 1.5 x 1.5 cm^2 pieces and then selectively etched, using a Kapton tape, with the solution of hydrogen peroxide (H_2O_2) and hydrochloric acid (HCL) (in a ratio of 1.0:1.0).

2.3.2 Cleaning of sITO substrates: After etching, sITO substrates were cleaned in an ultrasonic bath with detergent and ultrapure water at a temperature range of 22-23 ºC, followed by an acetone and isopropyl alcohol bath at a temperature of 150ºC and 180ºC, respectively. After the chemical cleaning, all the substrates were dried at 150°C for 20 minutes in a closed oven.

2.3.3 UV-ozone cleaning: Before the deposition of the ETL layer, the substrates went through UV-ozone cleaning for 15 min. The cleaning process helps to remove the organic impurities from the ITO surface and enhances the wettability of the substrates.

2.3.4 ETL deposition: The ZnO layer was deposited on sITO substrates with spin coating techniques (spun at 2500 rpm for 30 s with an acceleration of 1000 rpm). After coating, all the substrates were annealed at 150ºC for 15 min and left to cool down in open air.

2.3.5 Photoactive layer deposition: Before the deposition of the active layer, the solution of the photoactive layer was place on a hot plate with a temperature of 60ºC for 20-30 min and 450 rpm. The active layer, composed by a blend of P3HT:$PC_{61}BM$ with specific blend ratio, was deposited by dropping 40 µL and spinning for 40 s at 800 rpm, 1000 rpm, 1200 rpm, and 1500 rpm. Finally, the substrates were transferred to vacuum dry for 30 min and annealed for 10 min.

2.3.6 Deposition of the HTL (MoO_3): MoO_3 was deposit via Thermal Evaporation under high vacuum. The deposition was performed in a Modular Thin Film Deposition Systems HEX Series from Korvus Technology. The thin film of MoO_3 with a thickness of 8 -9 nm was deposited at a rate of 0.13 – 0.2 Å/sec under the vacuum pressure of 3.0E-06 mbar.

2.3.7 Deposition of top electrode (Ag): Sequentially, the top metal electrode (Ag) was deposited in the same thermal evaporated system. For the deposition of Ag, we have used molybdenum boat and all the samples were placed inside a shadow mask and positioned in the substrate holder (static). The deposition Ag performed at a rate of 0.1-0.6 Å/sec, to achieve a thickness of 150 nm.

2.4 Measurements and Characterization Techniques: A series of physical and chemical analytical techniques as well as electrical measurements were performed to analyze individual materials (P3HT:$PC_{61}BM$) and OSCs device performance.

2.4.1 UV-Visible Spectroscopy: The ultra-visible (UV-vis) absorption was measured by using a UV-Vis-NIR Spectrophotometer JASCO V-770, obtaining absorption with a FLH-740 Film holder (left spring type). The instrument is showed in Figure A7(e) in Appendix A.

2.4.2 Photoluminescence spectroscopy (PL): PL spectra of active layer thin films were obtained from an iHR320 fluorescence spectrometer. The results were recorded using the FluorEssence.

2.4.3 AFM spectroscopy: The atomic force microscopy (AFM) measurements were performed in an ALPHA RAS 300 operated in tapping mode (TM), using commercially available silicon AFM probes of 75 Hz (F=28 N/m). AFM was recorded in 3D and 2D images using WITec software. The instrument is showed in Figure A7(d), Appendix A.

2.4.4 Surface profilometry: The film thickness of the organic layer was measured using an AlphaStep D-600 Stylus profilometer from KLA Tencor. The average was calculated by taking several measurements at different film sections by carefully scratching off the organic layer alongside the substrate and recording height step. The instrument and the method are shown and described in Figure A7(i) and section A6 in Appendix A, respectively.

2.4.5 Electrical Characterization of OSCs: The *I-V* measurements were performed by a model 2410-C electrometer (Keithley), operated by a computer program connected to the GPIB-USB-HS board. The characteristics were recorded under the illumination of 100 mW/cm^2. Before the measurements, the intensity was calibrated with the power meter. The measurement setup is depicted in Figure A7(g) in Appendix A.

2.4.6 Electrochemical Impedance Spectroscopy (EIS): The impedance measurements were performed with a Potentiostat/galvanostat/ZRA 3000 from Gamry instruments equipped with a frequency analyzer module in the frequency range of 0.1 Hz - 1.0 MHz. AC oscillating amplitude was as low as 100 mV to maintain the linearity of the response, with a point increment of 10. All the devices used for this characterization were previously encapsulated using an encapsulation epoxy. The instrument setup is presented in Figure A7(j) in Appendix A.

Chapter 3: Results and Discussion

The main results obtained on the characterisation and measurements of BHJ polymer solar cells films & devices based on a blend of P3HT:PC$_{61}$BM are presented and discussed in this chapter. The chapter describes the optical characteristics (absorption spectrum and photoluminescence spectrum), morphological characteristics (topography results of AFM) and electrical characteristics (J-V characteristics, photovoltaic performance parameters and Impedance measurements of OSCs) of the devices. Here, electrical proprieties investigation is emphasized once this project aims to produce and investigate OSCs performance in the open air.

3.1 Optical Characterization:

The optical properties of the individual polymer and active layer (blend of pristine regioregular P3HT (rrP3HT) and PC$_{61}$BM in the 1,2-dichlorobenzene (o-DCB) solvent) are investigated by Ultraviolet-visible (UV-visible) and Photoluminescence (PL) spectroscopy techniques. The pristine polymer and active layer were spin-coated at 800 rpm, 1000 rpm, 1200 rpm and 1500 rpm at different concentration ratios, 1.0:0.6, 1.0:0.8 and 1.0:1.0 on ZnO coated sITO substrate. To fully understand its consequences, a brief description of both characterization techniques (UV-visible and PL) are introduced before each results' discussion.

3.1.1 UV-visible Absorption characterization:

Absorption measurement utilises the light energy between 200 to 800 nm and is separated into two regions, the ultraviolet (190 to 400 nm) and visible (400 to 800 nm) regions. [54] Whitin this range the absorption of ultraviolet or visible light energy by an organic semiconductor leads to a transition of an electron from LUMO level to HOMO level and generates excitons. [55]

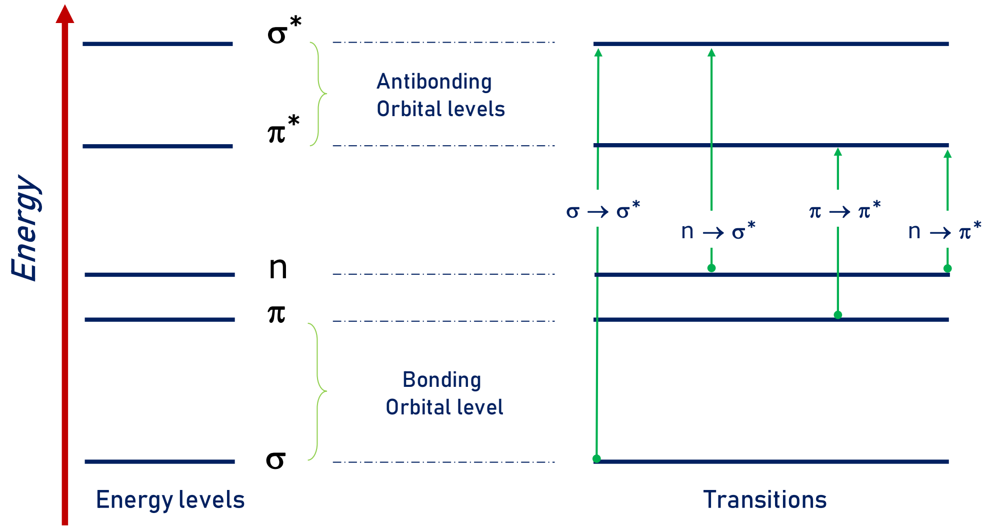

Figure 5 | Electronic transitions in UV-visible absorption spectroscopy.

The cause of these absorptions is associated with valance electron, which can be generally perceived in one of three types of electron orbitals: (1) single, or σ, bonding orbitals; (2) double or triple bonds (π bonding orbitals); and (3) nonbonding orbitals (lone pair electrons). When the incident electromagnetic radiation of the significant energy is absorbed by the organic semiconductor, a transition occurs from one of these orbitals to an empty orbital, usually referred as an antibonding orbital, σ^* or π^* (Figure 5). The precise energy differences among these orbitals depends on the atoms present and on the essence of the bonding system. Most of the transitions from bonding orbitals levels are of too high a frequency to measure easily, so most of the absorptions perceived include only $\pi \rightarrow \pi^*$, $n \rightarrow \sigma^*$, and $n \rightarrow \pi^*$ transitions. [56]

Absorption spectroscopy measures how much the light intensity is absorbed by an organic film over a range of wavelengths defined by the electromagnetic spectrum. For this purpose, the electromagnetic energy, emitted from the source (Tungsten and Deuterium lamp), was varied between the 300-700 nm, which corresponds to the ultraviolet and visible region. Therefore, by assuming that the loss of the intensity of light transmitted through an infinitesimally thin film is proportional to this intensity and the film thickness, the absorbance can be defined through the Lambert-Beer-Bouguer law, Equation 1. [57]

$$I(d) = I_0 \cdot \exp(-\alpha \cdot d) \qquad \textit{Equation } 1$$

$$\textit{where} \quad \alpha = \frac{1}{d} \times 2.303 \times \log_{10}\left(\frac{I_0}{I(d)}\right)$$

where, $\boldsymbol{I_0}$, $\boldsymbol{I(d)}$, $\boldsymbol{d}$ and $\boldsymbol{\alpha}$ represent the initial intensity of the light, light intensity after passing through the film, the thickness of the film and the Naperian absorption coefficient, respectively.

The UV-Vis absorption spectrum of individual P3HT polymer and P3HT:PC_{61}BM (polymer and acceptor) blend films prepared in DCB at various concentration with different spin-speeds (rpm) is illustrated in Figure 6. Figure 6(a) shows the absorption spectrum of pristine regioregular P3HT (rrP3HT) films with broad spectra from 400 nm to 650 nm, having two vibronic shoulders at 603 nm and 555 nm and an absorption peak at 523 nm. The vibronic shoulder at 555 nm and 603 nm are attributed to crystalline lamellae π-stacking order in P3HT films. [58] The absorption peak at 523 nm (photon energy of 2.37 eV) corresponds to π-π* transition (band-to-band) between the allowed highest occupied molecular orbital (HOMO) and the lowest unoccupied molecular orbital (LUMO) of P3HT film. [59] The absorption band edge of the P3HT films is observed at 658 nm with band energy of 1.89 eV. The reduction in absorption spectrum with an increase in spin-speed reveals the less absorption of photon energy, i.e. the lower the spin speed, the higher the thickness of P3HT films and more absorption of photons. Figure 6 (b), (c) and (d) demonstrate the absorption spectrum of P3HT:PC_{61}BM blend films at the wt.% concentration of 1.0:0.6, 1.0:0.8 and 1.0:1.0, respectively. In all the concentration, the spectra of P3HT:PC_{61}BM films show three absorption features, A at 603 nm, B at 555 nm and C at 527 nm, attributed to P3HT excitonic absorption with the contribution of Frankel excitons. The excitonic absorption A (603 nm) reveals the generation of singlet exciton, B (555 nm) indicates one exciton and one phonon generation and C (527 nm) related to the origination of one exciton plus two phonons. The absorption shoulder D at 320 to 350 nm indicates the contribution of $PC_{61}BM$ acceptor molecules. [59] The absorption spectrum of all the concentration follows the same trend, i.e. decrease in the absorption with an increase in the rpm speed (decrease in thickness of P3HT:$PC_{61}BM$ film). [60]–[62]

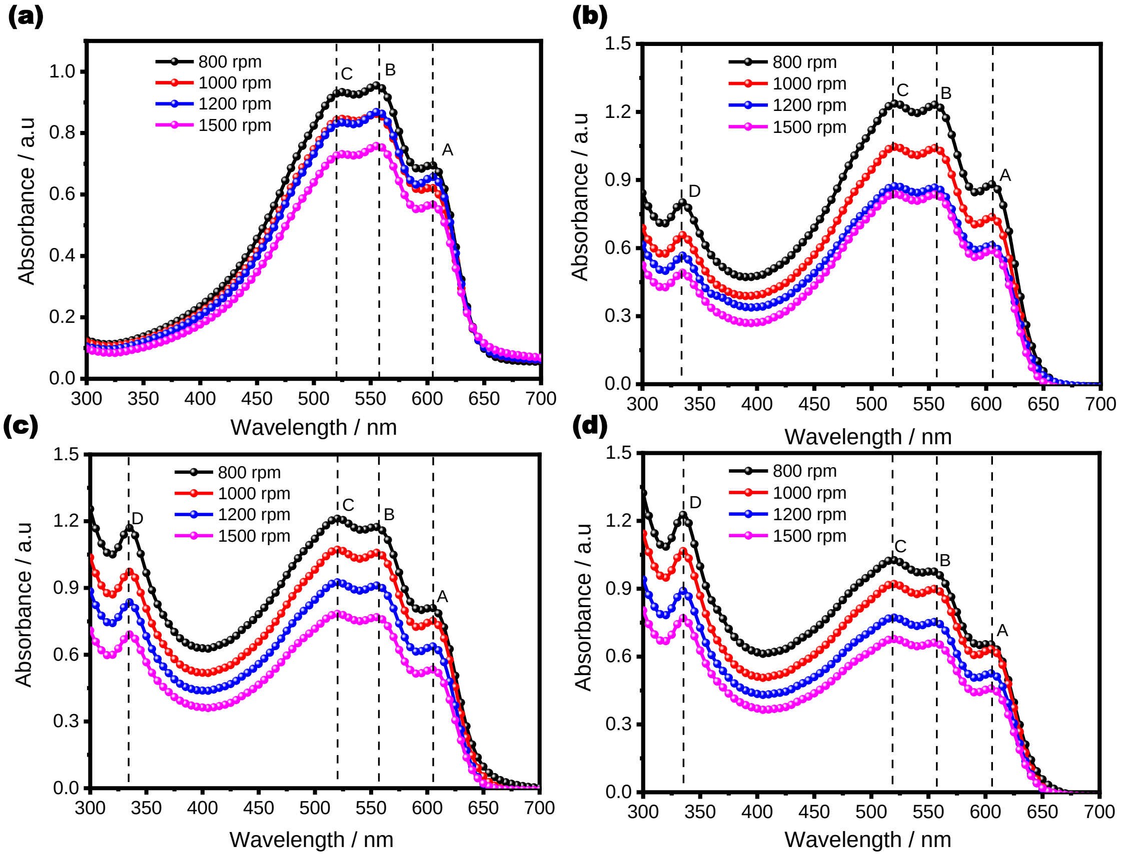

Figure 6 | Absorbance spectra of (a) pristine P3HT, (b) 1:0.6, (c) 1:0.8, and (d) 1:1 ratio coated at a spin-speed of 800 (black), 1000 (red), 1200 (blue) and 1500 rpm (pink).

Subsequently, the influence of $PC_{61}BM$ concentration on thin films absorption was investigated. Figure 8 (a), (b), (c) and (d) present P3HT:$PC_{61}BM$ thin films coated at 800 rpm, 1000 rpm, 1200 rpm and 1500 rpm, respectively, with a $PC_{61}BM$ composition of 1.0:0.6 (blue), 1.0:0.8 (red) and 1.0:1.0 (black) weight ratio. Figure 8 depicts the UV-visible absorption spectrum of P3HT: $PC_{61}BM$ film at different thickness with the variation of $PC_{61}BM$ in the P3HT: $PC_{61}BM$ blend ratios. These results reveal that in all the thicknesses, the variation of $PC_{61}BM$ concentration strongly influences the absorption intensity peak at 336 nm and absorption band 500 nm to 625 nm. The absorption peak at 336 nm increases with the increase in the concentration of $PC_{61}BM$ at all the thicknesses, which indicates a prominent peak of acceptor $PC_{61}BM$. The intensity of the absorption band from 500 nm to 625 nm (associated with P3HT polymer absorption) at 800 rpm and 1500 rpm shows the regular decrement with the increase in the concentration of $PC_{61}BM$. Nevertheless, in contrast at 1000 rpm and 1200 rpm the P3HT:$PC_{61}BM$ blend at 1.0:0.6 and 1.0:0.8

shows reverse nature in the absorption intensity from 500 nm to 625 nm. The change in the absorption spectrum from 500 nm to 625 nm could happen due to the influence of $PC_{61}BM$ on the slow growth of P3HT: $PC_{61}BM$ thin film formation, i.e. position and aggregation of $PC_{61}BM$ within the P3HT:$PC_{61}BM$ layer or variation in the reflectance of the thin film. [63]

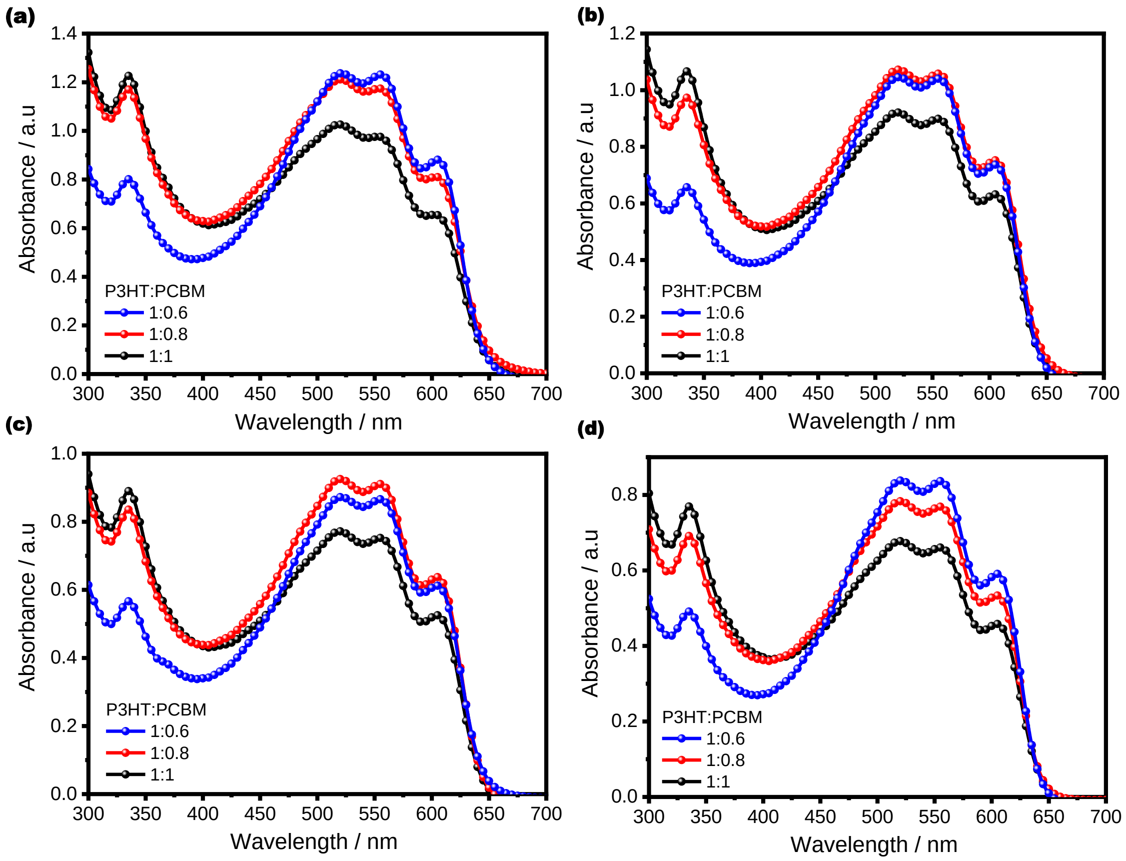

Figure 7 | Absorbance spectra of P3HT:PC61BM thin films coated at a spin-speed of (a) 800 rpm, (b) 1000 rpm, (c) 1200 rpm, and (d) 1500 rpm with a PC61BM composition weight ratio of 1.0:0.6 (blue), 1.0:0.8 (red) and 1.0:1.0 (black).

3.1.1 Photoluminescence (PL) characterization:

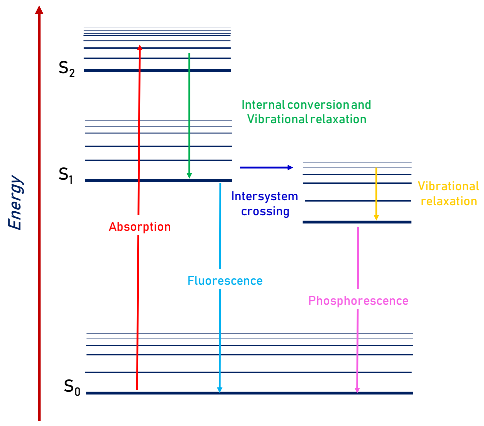

Figure 8 | Energy diagram showing the different mechanism involved in the light-matter interaction and different process involved in the photoluminescence of light.

Photoluminescence is a process in which an organic molecule absorbs a photon, having energy greater or equal to the bandgap of the organic molecule, and exciting one of its electrons to a higher energy state (S_2 transition state of LUMO level), and then emits a photon as the electron returns to its ground energy state (S_0 transition state of HOMO level). PL involves both fluorescence and phosphorescence processes and arises from an absorption/emission process among different electronic energy states in the organic molecule (Figure 8). [64] The PL intensity and kind of emission depend on the response of an organic molecule and on the wavelength of the light source. Undesired fluorescence intervention can ordinarily be shunned by keeping an appropriate light source (laser) wavelength. [65]

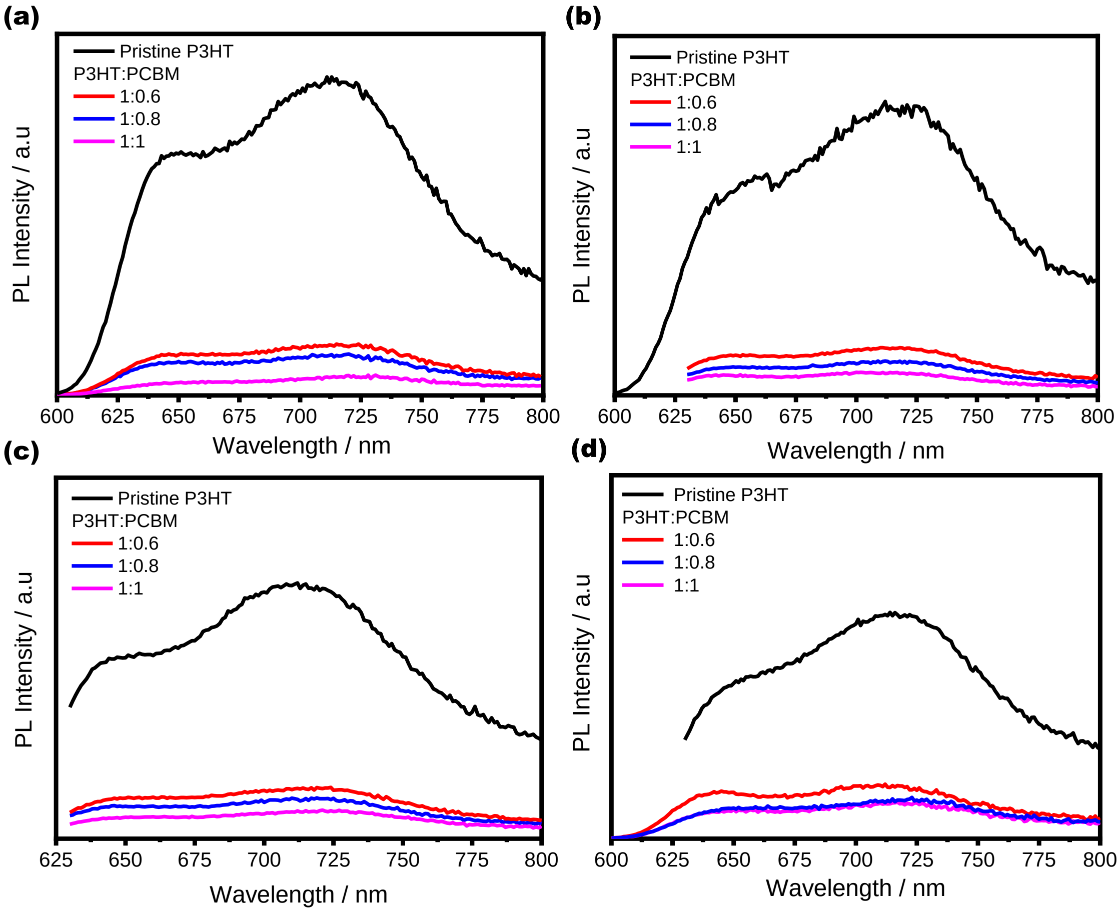

Figure 9 | PL spectrum of pristine rrP3HT and for P3HT:PC61BM thin films at different thickness (a) 800 rpm, (b) 1000 rpm, (c) 1200 rpm and (d) 1500 rpm.

If the organic molecule encounters internal energy redistribution after the initial photon absorption, the emitted photon is of lower energy than the absorbed photon. The PL spectroscopy has been a superior technique for optical characterization due to its non-destructive nature and ability to yield valuable information of intrinsic (e.g. carrier-carrier interaction) and extrinsic (e.g. defects) transitions. [66] In organic solar cells, PL study is used to understand the quenching and existence of intermolecular charge transfer between conjugated donor polymer and fullerene acceptor inside the blend system.

PL spectrum of pristine rrP3HT films at different thicknesses is shown in Figure 9. Figure 9 also yields different acceptor ($PC_{61}BM$) concentrations, namely 1.0:1.0 (pink), 1.0:0.8 (blue) and 1.0:0.6 (red), as function of different spin-speeds (800 rpm, 1000 rpm, 1200 rpm and 1500 rpm). Here, PL study is utilized to investigate the intermolecular charge transfer (CT) from rrP3HT polymer to $PC_{61}BM$ acceptor at different blend ratio. PL spectra of pristine rrP3HT thin films, prepared by spin-coating, are illustrated in Figure 9 (a), (b), (c) and (d) with a spin-speed of 800 rpm, 1000 rpm, 1200 rpm and 1500 rpm, respectively. Figure 9 (a), (b), (c) and (d) yield two vibronic peaks at 650 nm and 710 nm, which correspond to intra-chain and inter-chain radiative recombination of excitons in rrP3HT molecules, respectively. [67] These vibronic peaks are the result of the radiative transition of a P3HT electron, in the LUMO, to an unoccupied orbital, in the HOMO- radiative recombination. When rrP3HT is blended with $PC_{61}BM$, the PL intensity decreases as compared to pristine rrP3HT (black), which is designated as PL quenching. This phenomenon occurs due to the charge transfer from rrP3HT to $PC_{61}BM$ molecules. As the $PC_{61}BM$ concentration (60%, 80% and 100%) increases, more charges are transferred, instead of recombining; as a result, PL quenching is emphasized. [68] This trend is also observed in all the spin-speeds and concentrations, i.e. the fluorescence is further quenched with the increase of $PC_{61}BM$ concentration.

3.2 Morphological Characterization:

The morphology characterizations help to understand the phase separation of the donor and acceptor molecules, to investigate the morphology growth with various processing conditions involved in the film deposition, and then pave the approach for interpreting the property, morphology and performance relationship, which leads to the disposition of effective materials as well as the device design. The appropriate information of surface morphology, such as surface roughness, phase separation, surface composition, surface potential and so on, is normally elucidated via different characterization techniques like Optical Microscopy, Atomic Force Microscopy (AFM), Grazing Incidence X-ray Diffraction (GIXRD) or X-ray Photoelectron Spectroscopy (XPS) etc. [69] Among these characterization techniques, AFM is the most widely used characterization tool to understand the surface topography, phase separation between surface roughness of inorganic and organic thin films.

3.2.1 AFM Characterization:

AFM is a broadly used approach for surface morphology characterization of organic solar cells. It provides the primary erudition of surface morphology, mainly the surface topography (with high spatial resolution within 10 nm) and phase separation of donor-acceptor materials. [70] It should be perceived that the phase image is not the real phase separation image but illustrates

the variation in the stiffness on the surface of the sample. Moreover, the phase perception indicates the contrast in the phase of oscillations of the piezo-drive and the phase of actual oscillations of the AFM probe recorded by the photodetector. [71]

AFM has three different modes of operation, such as contact mode, tapping mode and non-contact mode; among these, tapping mode is commonly used to investigate the surface morphology of individual soft materials film. In tapping mode operation, the cantilever oscillates imperceptibly below to its resonant frequency. The amplitude of vibration is typically in the ranges from 20 - 100 nm. [72]The tip lightly "taps" on the surface of the film during the scanning process, contacting the surface at the bottom of its swing. Because the forces on the tip change as the tip-surface separation changes, the resonant frequency of the cantilever is dependent on this separation. The vibration is also damped when the tip reaches closely the sample surface. Hence the variations in the vibration amplitude can be used to estimate the distance between the tip and the surface. The feedback circuit adjusts the probe height to try and maintain a constant amplitude of vibration *(amplitude setpoint)*. [73]

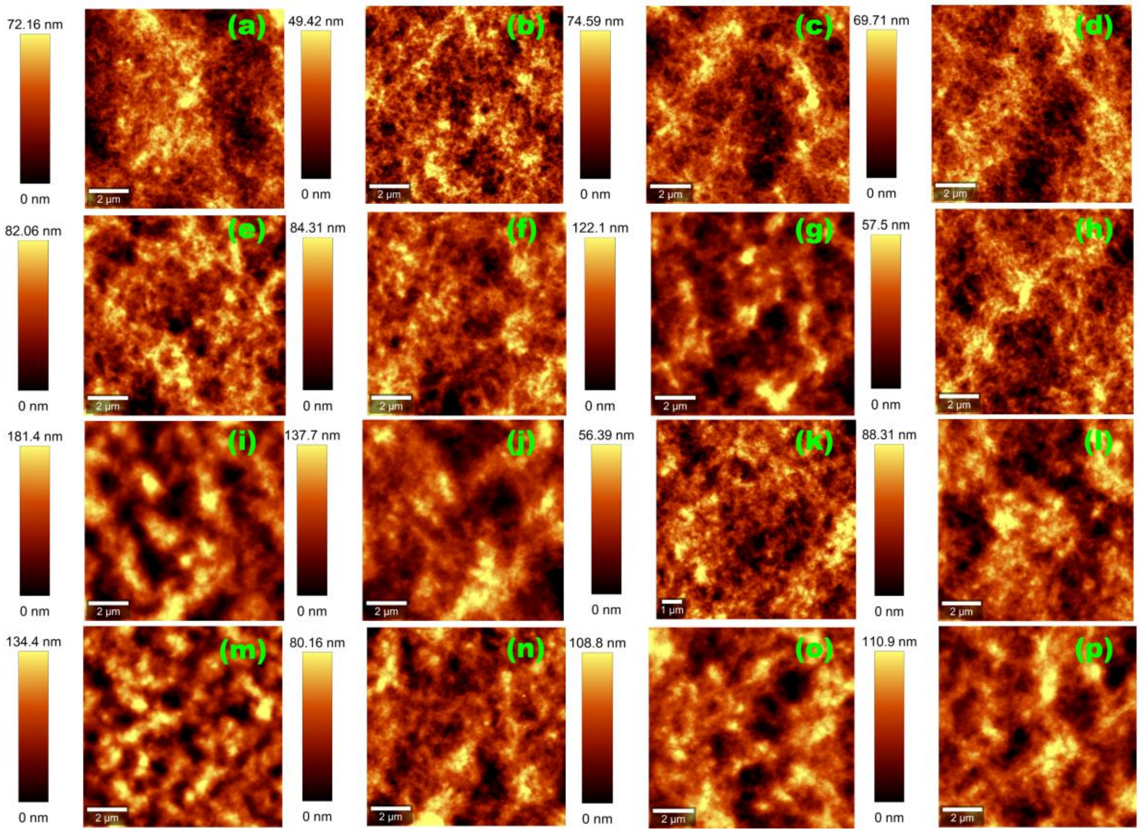

Figure 10 | AFM 2D topography images pristine rrP3HT coated at (a) 800 rpm, (c) 1000 rpm, (d) 1200 rpm and (c) 1500 rpm. rrP3HT:PC61BM with a PC61BM concentration of (e)-(h) 1.0:0.6, (i)-l) 1.0:0.8 and (m)-(p) 1.0:1.0, which posses the same rpm increment (800 rpm, 1000 rpm, 1200 rpm and 1500 rpm).

This section describes the tapping mode AFM study of sITO, ZnO, pristine rrP3HT films and rrP3HT:PC$_{61}$BM blend films (different thickness and blend ratio). A tapping mode operation is a successful approach to examine the surface properties of soft materials (polymers) thin film. Figure A2 shows the topography images of sITO deposited on a glass substrate and ZnO film spin-casted on sITO coated glass substrate. The root mean square roughness (R$_{rms}$) of cITO and ZnO films is listed in Table 1. Figure A2 and Table 1 clearly illustrate that the deposition of ZnO film on the sITO improves the surface morphology and reduces the roughness (from 4 nm to 3 nm) of the overall film, respectively.

The topography 2D images of P3HT and P3HT:PC$_{61}$BM films spin-coated on ZnO deposited sITO substrates (at different spin-speed and PC$_{61}$BM concentration) are shown in Figure 10. Figure 10 (a), (b), (c) and (d) demonstrate the surface morphology of P3HT thin films deposit at a spin-speed of 800 rpm, 1000 rpm, 1200 rpm and 1500 rpm, respectively, with a correspondent thickness of 16 nm, 10 nm, 16 nm and 16 nm, which are listed in Table 1. The topography images of rrP3HT matrix show higher (bright) and lower (dark) morphology, which is attributed to the hard regions of the polymer crystallites due to the self-organized polymer chains within the film. [74]These regions are formed by a closely packed chain (crystalline domains), which is interspersed by amorphous regions (do not possess a proper chain stacking). [74] Correlating the AFM topography images with the surface roughness values, a reasonably homogenous surface is achieved for all the spin-speeds, without significant roughness changes with the increase of the spin-speed.

Table 1 | Root mean square roughness (Rrms) values of films used in the fabrication of OSCs devices such as sITO, ZnO, pristine P3HT, and P3HT:PC$_{61}$BM blend films.

Sample description/ Deposition technique, blend ratio, material wt%	Sample thickness / spin speed (rpm)	Surface Roughness (Rrms in nm)
sITO film deposited by Sputtering	≈ 130 nm	4
ZnO NPs film deposited on sITO with the spin casting method	2500 rpm	3
P3HT polymer film deposit on ZnO coated sITO substrate with the spin casting method. The wt% of P3HT polymer is **30 mg/ml** in o-DCB solvent	800 rpm	16
	1000 rpm	10
	1200 rpm	16
	1500 rpm	16
P3HT:PC$_{61}$BM polymer film deposit on ZnO coated sITO substrate with the spin casting method. The blend ratio of P3HT:PC$_{61}$BM is **1.0:0.6** at wt% of **30 mg/ml** in o-DCB solvent	800 rpm	26
	1000 rpm	17
	1200 rpm	12
	1500 rpm	18
P3HT:PC$_{61}$BM polymer film deposit on ZnO coated sITO substrate with the spin casting method. The blend ratio of P3HT:PC$_{61}$BM is **1.0:0.8** at wt% of **30 mg/ml** in o-DCB solvent	800 rpm	30
	1000 rpm	17
	1200 rpm	25
	1500 rpm	24
P3HT:PC$_{61}$BM polymer film deposit on ZnO coated sITO substrate with the spin casting method. The blend ratio of P3HT:PC$_{61}$BM is **1.0:1.0** at wt% of **30 mg/ml** in o-DCB solvent	800 rpm	42
	1000 rpm	30
	1200 rpm	12
	1500 rpm	20

The surface morphology of P3HT:$PC_{61}BM$ thin films in a blended system of 1.0:0.6, 1.0:0.8 and 1.0:1.0 are shown in Figure 10 (e)-(h), (i)-(l) and (m)-(p), respectively, deposit at a spin-speed of 800 rpm, 1000 rpm, 1200 rpm and 1500 rpm. From these topography images, it is possible to observe the appearance of nanocluster after blended P3HT with $PC_{61}BM$, which results from the aggregation of $PC_{61}BM$ during the slow growth of blend film; consequently the surface morphology changes. Moreover, a hill-like (in 3D images, Figure A.3 illustrated in section A3 from Appendix A) feature is consistent in all the topography images. However, a more homogenous hill-like texture is grown at a speed-spin of 1200 rpm in all the ratios. The formation of a smooth surface is a critical OCSs requirement once it yields increase: interfacial contact between the P3HT:$PC_{61}BM$ layer and the MoO_3/Ag layer, and the separation of photogenerated electron and hole pairs at the active layer interface. [75]

Concerning $PC_{61}BM$ weight (wt.%) content, as it decreases, an undesirable distribution of P3HT at the interface of P3HT: $PC_{61}BM$ and MoO_3 is expected. [74], [75] When comparing the AFM surface images of P3HT:$PC_{61}BM$ with a $PC_{61}BM$ concentration of 60% (1.0:0.6), 80% (1.0:0.8) and 100% (1.0:1.0), the density and size of $PC_{61}BM$ clusters (crystal grains), which are formed after slow growth and annealing process, are more extensive, 80% and 100%, respectively.

3.3 Electrical characterization:

In this section, a comprehensive electrical analysis will be conducted through the photovoltaic characterization of OSCs under dark and light conditions. Moreover, electrochemical impedance spectroscopy (EIS) was used to understand the charge transport mechanism of air processed OSCs devices and to extract valuable information on OSCs behaviour under dark and light conditions.

3.3.1 Current density vs Voltage measurements of OSCs devices:

The current density vs voltage (*J-V*) characteristics is a primary technique for the characterization of solar cells devices. The solar cell performance parameters, such as short-circuit current density (J_{SC}), open-circuit voltage (Voc), Fill Factor (FF) and power conversion efficiency (PCE) along with series resistance (R_S) and shunt resistance (R_{SH}), are easily extracted from the interpretation of the *J-V* characteristics. These characteristics can be measured under dark or light with the standard illumination intensity of 100 $mWcm^{-2}$ (AM 1.5).

Figure 11 illustrates the *J-V* characteristics of four OSCs devices fabricated in an inverted configuration viz. sITO/ZnO/P3HT:$PC_{61}BM/MoO_3$/Ag with different blend ratios (1.0:0.6, 1.0:0.8 and 1.0:1.0) coated at a spin-speed of 800 rpm, 1000 rpm, 1200 rpm and 1500 rpm. The photovoltaic parameters from the best-produced devices are listed in Table 2, and the respective average and standard deviation are registered in Table 3. The *J-V* characteristics measured in the dark are represented in A.4, Figure A4 in section of appendix A.

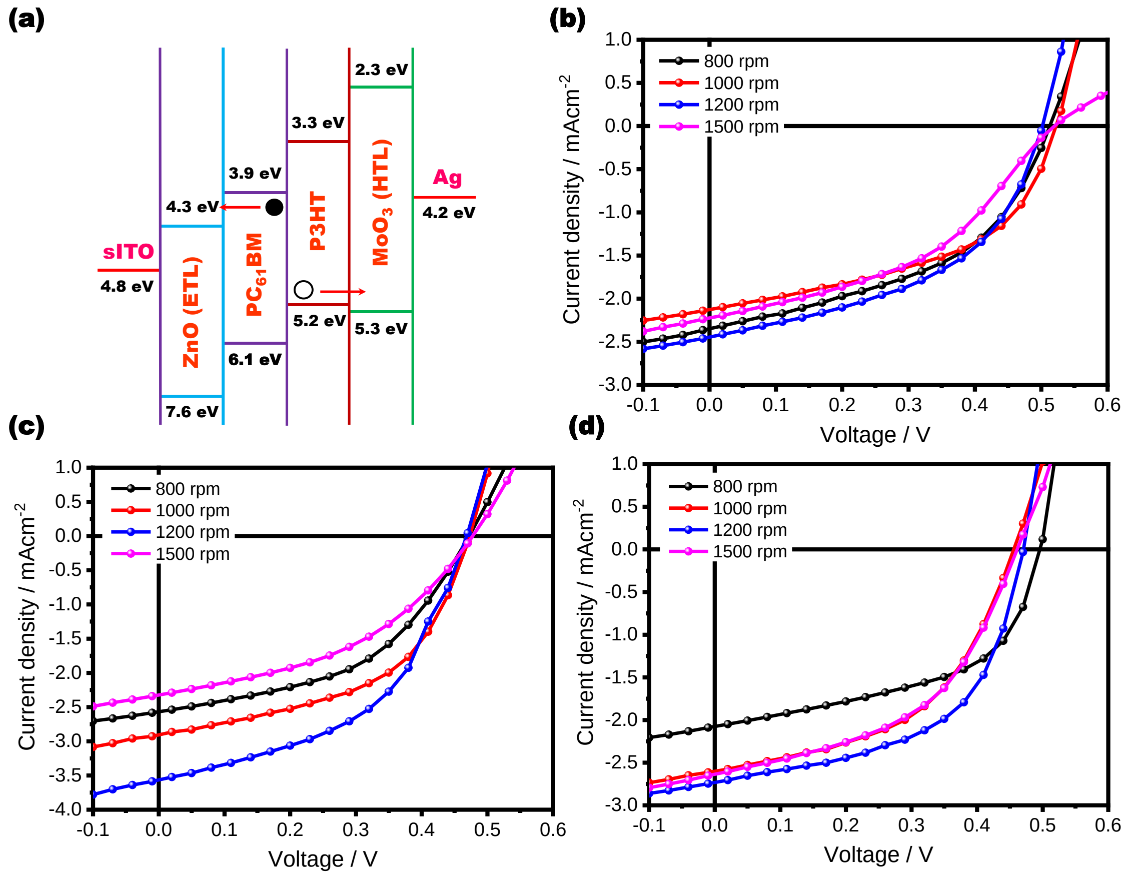

Figure 11 | Energy band diagram (a) and *J-V* characteristics of proposed devices at different blend ratio of (b) 1.0:0.6, (c) 1.0:0.8 and (d) 1.0:1. In all the systems, the photoactive layer was coated at a speed-spin of 800 rpm (black), 1000 rpm (red), 1200 rpm (blue) and 1500 rpm (pink) under a light intensity of 100 mWcm^{-2}

Table 2 | Photovoltaic performance parameter of proposed air processed inverted OSCs devices.

P3HT:PC$_{61}$M Blend ratio	Spin speed	Voc (V)	Jsc (mAcm-2)	FF (%)	PCE (%)	R_S (Ωcm^2)	R_{SH} (Ωcm^2)
1.0:0.6	800 rpm	0.51	2.35	46	0.56	50	568
	1000 rpm	0.52	2.13	49	0.54	36	719
	1200 rpm	0.50	2.45	48	0.58	47	649
	1500 rpm	0.52	2.20	42	0.49	161	641
1.0:0.8	800 rpm	0.47	2.57	47	0.57	56	662
	1000 rpm	0.47	2.91	51	0.7	34	658
	1200 rpm	0.47	3.56	48	0.81	33	476
	1500 rpm	0.48	2.28	45	0.49	70	606
1.0:1.0	800 rpm	0.48	2.62	47	0.59	26	725
	1000 rpm	0.46	2.53	50	0.59	47	741
	1200 rpm	0.47	2.73	54	0.70	26	680
	1500 rpm	0.48	2.64	49	0.30	53	680

Table 3 | Average and standard deduction values of a photovoltaic performance parameter of proposed air processed inverted OSCs devices. (average of the results obtained from 10 devices)

P3HT:PC_{61}BM Blend ratio	Spin speed	V_{OC} (V)	J_{SC} (mA/cm^2)	FF (%)	PCE (%)
1.0:0.6	800 rpm	0.51 ± 0.006	2.29 ± 0,150	45 ± 1.85	0.51 ± 0.032
	1000 rpm	0.52 ± 0.004	2.00 ± 0.111	48 ± 1.81	0.46 ± 0.036
	1200 rpm	0.50 ± 0.032	3.17 ± 0.908	40 ± 4,58	0.56 ± 0.161
	1500 rpm	0.52 ± 0.005	2.18 ± 0.042	42 ± 0.58	0,48 ± 0.014
1.0:0.8	800 rpm	0.47 ± 0.008	2.53 ± 0.025	45 ± 1.51	0,54 ± 0.019
	1000 rpm	0.48 ± 0.005	2.77 ± 1.057	49 ± 1.10	0.66 ± 0.021
	1200 rpm	0.48 ± 0.005	2.70 ± 0.383	51 ± 1.30	0.67 ± 0.064
	1500 rpm	0.49 ± 0.016	2.06 ± 0.235	46 ± 1.26	0.45 ± 0.235
1.0:1.0	800 rpm	0.48 ± 0.017	2.87 ± 0.689	47 ± 3.37	0.59 ± 0.216
	1000 rpm	0.46 ± 0.008	2.34 ± 0.221	51 ± 3.14	0.58 ± 0.080
	1200 rpm	0.49 ± 0.010	2.60 ± 0.083	49 ± 3.84	0.59 ± 0.052
	1500 rpm	0.46 ± 0.461	2.15 ± 0.400	49 ± 3.52	0.48 ± 0.087

From the OPVs summary photovoltaic parameters, displayed in Table 2, it is possible to recognize that for a blend system of 1.0:0.6, the best PCE value is 0.58 %, resulting from an arrangement of the open-circuit (V_{OC}), short circuit current density (J_{SC}), fill factor (FF), series resistance (R_S) and shunt resistance (R_{SH}) of 0.50 V, 2.45 mAcm^{-2}, 48 %, 46.62 Ωcm^2 and 649.35 Ωcm^2, respectively. For a ratio of 1.0:0.8 the photovoltaic parameters, V_{OC}, J_{SC}, FF, R_S and R_{SH}, are 0.47 V, 3.56 mAcm^{-2}, 48%, 33.12 Ωcm^2 and 476.19 Ωcm^2, resulting in a PCE of 0.81 %. In contrast, for a blend system of 1.0:1.0, the highest PCE obtained is 0.70 %, which results in 0.47 V, 2.17 mAcm$^{-2,}$ 54 %, 26.12 Ωcm^2 and 680.27 Ωcm^2. In all the blend systems, the highest recorded PCE was consistently achieved at a spin-speed of 1200 rpm.

Therefore, from the presented results, some important considerations can be made. The J_{SC} of the produced devices increased gradually until an active layer thickness of ~217 nm (1200 rpm). This is because there is an intrinsic relation between the active layer thickness, exciton diffusion length, which is an inherent characteristic of the material in the study, and the light absorption. As the active layer thickness increases, the light absorption increases too, although the recombination rate rises due to the fact the excitons (bound state of an electron and an electron-hole) are not able to reach a donor/acceptor (D/A) interface to dissociate, due to large phase separations as compared to the electron diffusion length, reducing J_{SC}. [61]As regards to FF, this also decreases when the photoactive thickness is more extensive or lower than the optimal thickness. [76]Furthermore, this parameter is closely related to R_S and R_{Sh}. The R_S is linked to the intrinsic resistance, polymer-metal interface morphology, and thickness of the photoactive layer. [77]In Table 2, it is possible to observe that the highest R_S value was 161 Ωcm^2, for a blended system of 1.0:1.0 and a spin-speed of 1000 rpm, which indicates a high recombination rate[76]In contrast, R_{SH} is related to the amount and character of impurities and defects present in the active layer. [76]In this study, the lowest R_{SH} value, which was 476 Ωcm^2, was found at a 1.0:1.0 ratio with a spin-speed of 1200 rpm. This indicates that the produced film possesses high charge recombination and leakage current.[78]Thus, it is possible to remark that as the thickness increases, the R_S increases and the R_{SH} decreases, resulting in a reduction of FF. Regarding to V_{OC}, the OSCs presented a similar value ~0.49 V, because this photovoltaic parameter is mainly dominated by the difference between the HOMO, level of rrP3HT (donor), and LUMO, level of $PC_{61}BM$ (acceptor). [79]

With the purpose of better visualize the previously reported considerations, four comparison graphics were plotted, - V_{OC}, J_{SC}, FF, and PCE vs spin-speed. The resulting graphics are illustrated in Figure 12.

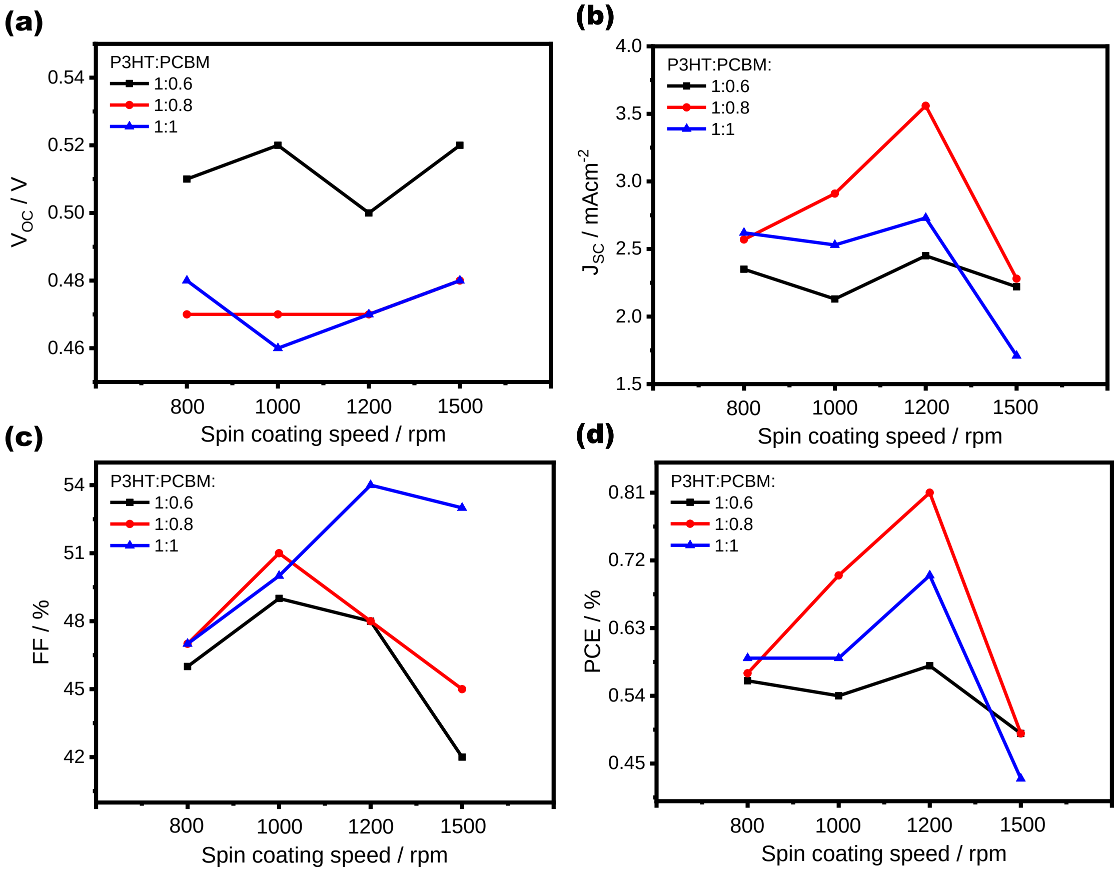

Figure 12 | Spin-speed dependence of (a) V_{OC}, (b) J_{SC}, (c) FF, (d) PCE for a blend system of 1.0:0.6 (black), 1.0:0.8 (red) and 1.0:1.0 (blue) for the OPV devices under light conditions.

Besides the active layer thickness, the D/A ratio is of key importance. Therefore, it is necessary to understand which rrP3HT:$PC_{61}BM$ blend system is most suitable to improve the device performance. To facilitate the perception, four comparison graphics were plotted. The V_{OC}, J_{SC}, FF, and PCE vs $PC_{61}BM$ weight (wt.%) ratio are illustrated in Figure 12 (a), (b), (c), and (d), respectively.

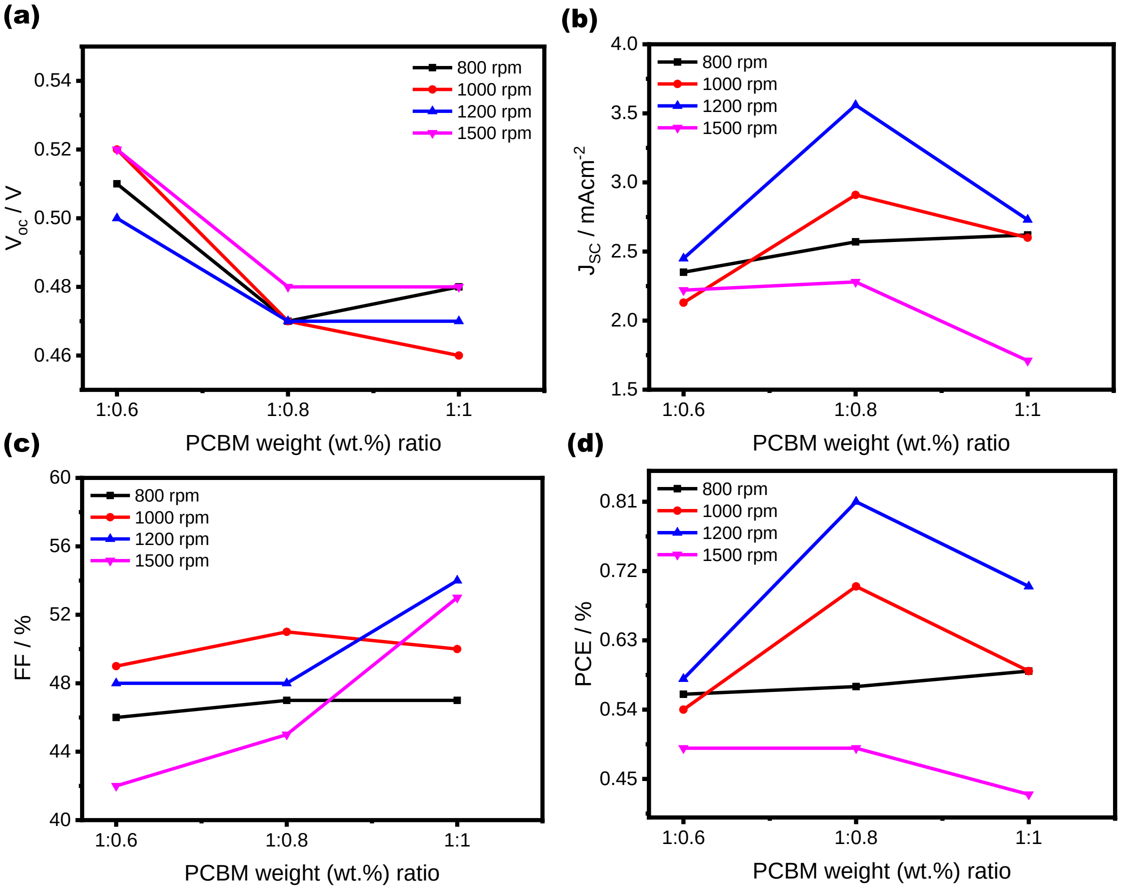

Figure 13 | $PC_{61}BM$ weight (wt.%) ratio dependence of (a) V_{OC}, (b) J_{SC}, (c) FF, (d) PCE for a blend system at a spin-speed of 800 rpm (black), 1000 rpm (red), 1200 rpm (blue), 1500 rpm (pink).

Figure 13 corroborates the previous statements. There have not been any significant changes on V_{OC} (Figure 13a), once the materials used in the photoactive layer were the same, which did not contribute to alterations on HOMO and LUMO energy level alignment of rrP3HT and $PC_{61}BM$, respectively. There are also no sharp variations in FF (Figure 13c). As regards to J_{SC} (Figure Xb), less recombination losses are visible for a blended system of 1.0:0.8 at a spin-speed of 1200 rpm, increasing J_{SC}. As a general point of view, taking in consideration Figure 13, it can be experiential that at blend system ratio is 1.0:0.8 the photovoltaic parameters are enhanced, namely PCE.

3.3.2 Impedance measurement of OSCs devices

Impedance spectroscopy (IS) is a broadly used approach to investigate the charge transport mechanism of all types of solar cells devices, such as silicon solar cells, dye-sensitized solar cells (DSSC), organic solar cells, and perovskite solar cells. This technique involves the utilization of a small AC perturbation (Vac) signal modulated with DC polarization voltage (V_{DC}), which is applied to solar cell devices and measuring the analogous current density response (Jac) superimposed on the steady-state current density (J_{DC}). [80]

$$Z(\omega) = \frac{V}{J} = Z_0 \cdot \exp(j\phi) = Z_0 \left(\cos\phi + j\sin\phi\right)$$

In the expression of an impedance transfer function, *Z (ω)* is represented in the form of real (Z´) and an imaginary part (Z”). If we plot the real part of the impedance on the X-axis and the corresponding imaginary part on the Y-axis over a range of measured frequency (for OSCs mHz to 1 MHz), we can get a plot called “Nyquist Plot” (Figure 14). [81] In general, if the performance of the OSCs device is purely resistive-capacitive, the Y-axis presents the opposite of the imaginary part. The obtained Nyquist Plot is attributed to the graphical illustration of various internal mechanistic processes happening on different characteristic timescales. Moreover, these characteristic timescales can be modelled as a combination of passive electrical elements that yield time constants. These passive electrical elements are the models of physical mechanisms occurring inside the OSCs, such as diffusion, recombination and charge storage etc. [82],[83]

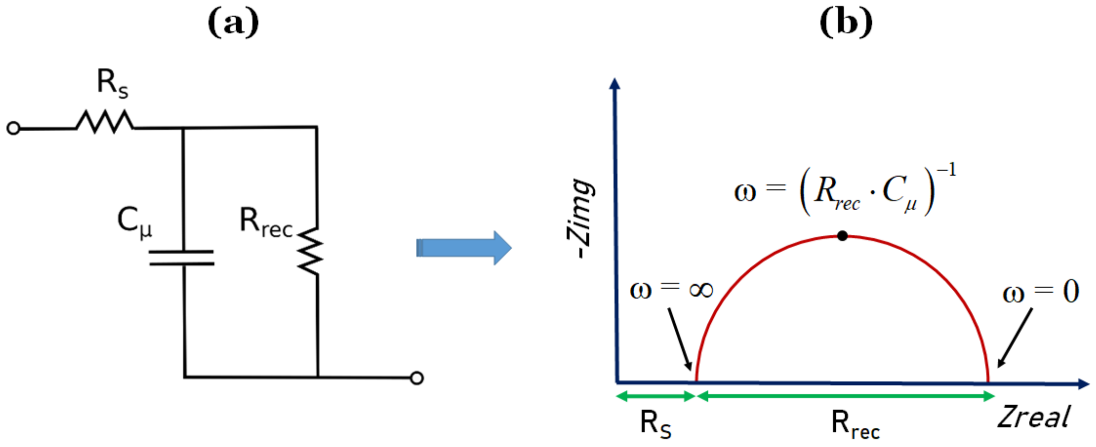

Figure 14 | Electrical model and Nyquist plot (a) Basic solar cell electrical model (b) graphical representation of Z-plane response.

Figure 14 presents the primary solar cell model that consists of a series resistance R_S (resistance offered by electrode), in series with the parallel combination of the chemical capacitance C_μ (filling of the density of states of the active layer) and recombination resistance R_{rec} (depicts the density of recombination of charge carriers). [82] The graphical outcome of the impedance response of the solar cell device consists of an arc in the upper quadrant whose diameter is given by R_{rec} and which is displaced along the x-axis by a value equal to R_S. [82] Moreover, the maxima of the imaginary impedance at a specific angular frequency (a black point on the top of arc) corresponds to the inverse of the characteristic time constants (product of R_{rec} and C_μ). In general, these characteristic time constants can help to extract valuable information about fundamental mechanisms in the solar cell.

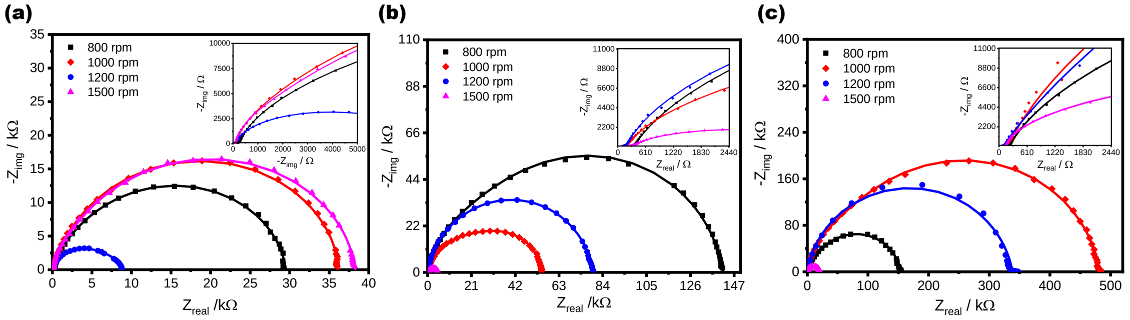

Figure 15 | Nyquist polt with model fitting of air processed P3HT:PC$_{61}$BM based OSCs fabricated on various thicknesses (800 rpm, 100 rpm, 1200 rpm, and 1500 rpm) at specific blend ratio (a) 1.0:0.6 (b)-d) 1.0:0.8 and (c) 1.0:1.0 under Dark conditions.

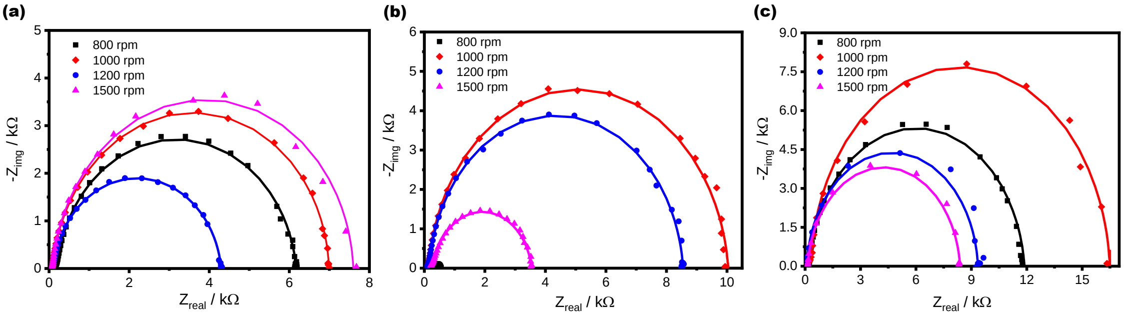

Figure 16 | Nyquist polt with model fitting of air processed P3HT:PC$_{61}$BM based OSCs fabricated on various thicknesses (800 rpm, 100 rpm, 1200 rpm, and 1500 rpm) at specific blend ratio (a) 1.0:0.6 (b)-d) 1.0:0.8 and (c) 1.0:1.0 under Light conditions (100 mWcm^{-2})

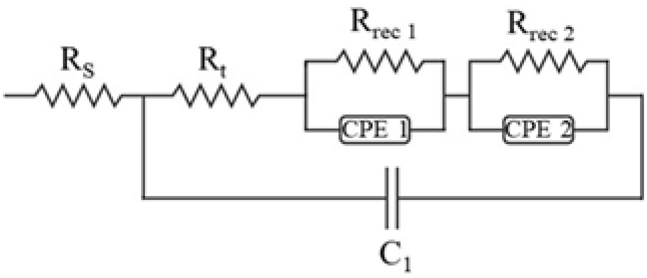

Figure 17 | Electrical model for air processed OSCs designed by the fitting of Nyquist plots under dark and light conditions

In this work, we have obtained Nyquist plots of the air processed bulk heterojunction organics solar cell at different blend ratio with various thicknesses. These Nyquist plots have measured in the dark as well as in the light, as shown in Figures 15 and 16, respectively, and these impedance spectra show the combination of two semi-circles: the first lies in the low-frequency region and the second is located at high frequencies. [84] The appearance of two semicircles is related to electrical transport processes (relaxation processes). Based on the analysis of the obtained Nyquist Plots, we have designed an electrical model of air processed inverted OSCs (blend of P3HT:PC$_{61}$BM). This electrical model is a combination of series resistances (R_s), charge transfer resistance (R_t), capacitances (C), and two parallel combinations of recombination resistance and constant phase element (R_{rec2}||CPE_2 in series to R_{rec1}||CPE_1); the equivalent circuit of air processed OSCs is shown in Figure 17. The R_S is associated with the (ohmic) resistance from the contact layers and electrodes. [80] The electrical resistance of the interface ZnO (ETL) and the photoactive layer is designated as R_t. In contrast, R_{rec1} and R_{rec2} are related rrP3HT:PC_{61}BM BHJ resistance and rrP3HT:PC_{61}BM layer and the MoO_3/Ag interface, respectively. [85]Moreover, a CPE_1 and CPE_2 are linked to the formation of a depletion layer in the ETL and photoactive layer, respectively. [86] The CPE was used to describe the inhomogeneous and grain boundaries (e.g., porosities, surface states) features of BHJ active layer and from CPE values (obtained from model fitting), we can easily evaluate the chemical capacitance (Cµ, which reflects carrier accumulation in the bulk active layer) by using the equation [87]:

$$C\mu = \frac{\left(Y_0 \cdot R_{rec}\right)^{1/n}}{R_{rec}}$$

where Y_0 and n are the parameters associated with CPE, and are obtained using the fitting of Nyquist plot with the electrical model. To determine the characteristic time constants related to electron diffusion, i.e., diffusion time/transit time and relaxation time/effective lifetime, the chemical potential ($C\mu$) is used in the following equation. [88], [89]

$$\tau_d = R_t \cdot C_\mu$$

$$\tau_n = R_{rec} \cdot C_\mu$$

From this transit time, we can easily calculate the electron diffusivity (chemical diffusion coefficient) and electron mobility by using the Nernst–Einstein relationship. [82], [89]

$$D_n = \frac{L^2}{\tau_d} \quad \rightarrow \quad \mu_n = \frac{e \cdot D_n}{k_B \cdot T}$$

where the D_n is the diffusion coefficient, μ_n is the electron mobility, e is the electronic charge and k_BT is the thermal energy (25.7 meV). From these equations, we can calculate all the parameters associated with the charge transport mechanism. In the electrical modelling of air processed inverted OSCs, we obtained two chemical capacitance ($C\mu_1$, $C\mu_2$), associated with two relaxations/effective lifetime (τ_1 high-frequency region and τ_2 to the low-frequency region, which results in a low τ_1 and high τ_2 fast and slow process during the charge transport). All the obtained parameter and calculated values, under dark and light conditions, are illustrated in Table 4 and Table 5, respectively. From these Tables' analysis, it is possible to observe that R_S is not consistent in the devices, which is attributed to sITO. Parameters such as sheet resistance (R_S) and conductivity (σ) of sITO and commercial ITO differ, due to the nature of the grain size and grain boundaries. For example, the RF sITO produced, in this work, achieved an R_S of 150 Ωcm^{-1}, in contrast to a much lower value in commercial ITO, 36 Ωcm^{-1}. Furthermore, the conductivity on sITO and commercial ITO are 3.51×10^{2} $\Omega^{-1}cm^{-1}$ and 1.9×10^{3} $\Omega^{-1}cm^{-1}$, respectively. [90] Therefore, the electrical device parameters will be affected not just by the difference of the parameters, but also by the varying grain size and boundary during its fabrication.

Blend system	**Spin speed/ rpm**	**R_S / Ω**	**R_{rec1} / Ω**	**R_{rec2} / Ω**	**R_t / Ω**	**CPE_1 / F**	**CPE_2 / F**	**τ_{n1} / s**	**τ_{n2} / s**	**τ_d / s**	**μ_n / $cm^2V^{-1}s^{-1}$**
1:0.6	800	157	4598	24500	256	1,77E-08	1,09E-08	8,16E-05	2.67E-03	4,54E-06	7,06E-03
	1000	64	3608	32430	118	2,07E-08	2,38E-08	7,48E-05	7,73E-04	2,44E-06	6,69E-03
	1200	82	6121	2265	354	2,41E-09	1,99E-09	1,48E-05	4,52E-06	8,53E-07	1,57E-02
	1500	68	32130	5820	273	7,40E-09	6,07E-09	2,38E-04	3,53E-05	2,02E-06	4,86E-03
1:0.8	800	198	25850	115300	296	6,89E-09	3,66E-08	1,78E-04	4,21E-03	2,04E-06	1,66E-02
	1000	98	27410	26720	435	8,04E-09	8,03E-09	2,20E-04	2,14E-04	3,50E-06	6,00E-03
	1200	78	5526	73230	271	1,02E-08	1,36E-08	5,64E-05	9,96E-04	2,76E-06	6,64E-03
	1500	210	4559	113	243	1,21E-09	5,08E-09	1,66E-06	1,50E-03	2,28E-07	6,40E-02
1:1	800	60	13260	203300	155	7,19E-09	9,90E-09	9,53E-05	1,31E-04	1,11E-06	3,49E-02
	1000	75	44420	16770	409	5,23E-10	3,95E-10	2,35E-05	6,62E-06	2,16E-07	1,22E-01
	1200	51	11280	320100	113	4,24E-08	4,93E-08	4,78E-04	1,58E-02	4,78E-06	4,94E-03
	1500	113	17410	1227	152	3,86E-09	2,80E-09	6,71E-05	3,44E-06	5,85E-07	3,13E-02

Table 4 | Impedance parameters calculated through the proposed Electrical Model under dark conditions.

Blend system	**Spin speed/ rpm**	**R_S / Ω**	**R_{rec1} / Ω**	**R_{rec2} / Ω**	**R_t / Ω**	**$C\mu_1$ / F**	**$C\mu_2$ / F**	**τ_{n1} / s**	**τ_{n2} / s**	**τ_d / s**	**μ_n / $cm^2V^{-1}s^{-1}$**
1:0.6	800	133	5878	2256	160	4,68E-09	4,22E-09	2,75E-05	2,45E-05	7,49E-07	4,28E-02
	1000	74	1099	5733	83	3,16E-08	3,33E-08	3,47E-05	1,91E-04	2,61E-06	6,25E-03
	1200	81	3988	7.305	278	8,39E-09	7,34E-09	5,56E-05	3,15E-06	1,68E-06	7,95E-03
	1500	70	4249	3077	203	1,52E-08	1,52E-08	6,45E-05	4,67E-05	3,08E-06	3,18E-03
1:0.8	800	199	2378	8290	114	8,58E-10	3,40E-09	2,04E-07	8,08E-07	9,76E-08	3,47E-01
	1000	92	9761	6868	190	7,08E-09	7,01E-09	6,91E-05	4,81E-05	1,35E-06	1,56E-02
	1200	75	77	8271	125	1,03E-07	1,43E-07	7,93E-06	1,18E-03	1,29E-05	1,42E-03
	1500	197	3110	8428	233	8,04E-09	8,78E-09	2,50E-05	7,40E-05	1,88E-06	7,76E-03
1:1	800	40	9596	3590	248	1,94E-09	1,78E-09	1,86E-05	6,40E-06	4,82E-07	8,04E-02
	1000	88	293700	12870	253	3,91E-09	3,08E-09	1,15E-03	3,96E-05	9,89E-07	2,65E-02
	1200	59	9100	11590	194	7,81E-09	7,81E-09	7,10E-05	9,05E-05	1,51E-06	1,56E-02
	1500	113	7723	2662	179	1,34E-09	1,12E-09	1,05E-05	2,97E-06	2,43E-07	7,54E-02

Table 5 | Impedance parameters calculated through the proposed Electrical Model under Light conditions (100 $mWcm^{-2}$).

3.3.3 Stability measurement of encapsulated air processed OSCs devices:

As previously discussed in the introduction, OSCs are a promising technology for light-harvesting, although the efficiency and stability are still low as compared to the inorganic counterparts. Studies on OSCs stability, which are essential for technological applications, are manlily conducted in encapsulated devices by ageing acceleration under laboratory conditions. Once the organic materials are by nature more physical (e.g., morphology stability) and chemical (e.g., oxygen, water and UV radiation) susceptible to degradation, performing encapsulation is essential to prevent it. [91], [92]

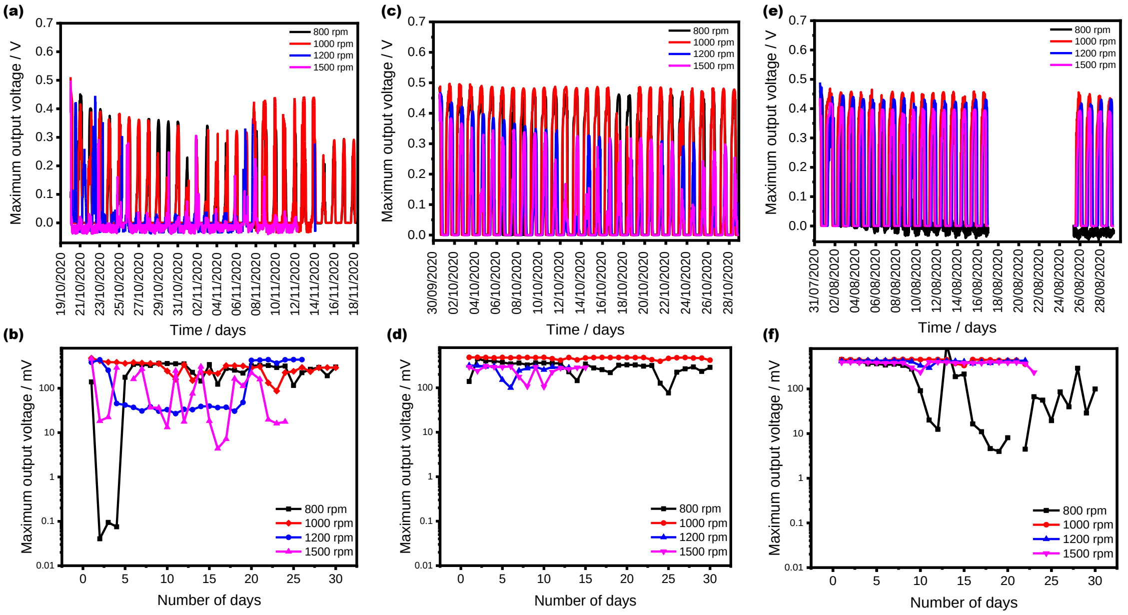

Figure 18 | Stability study of encapsulated air process OSCs by Maximum Output Voltage vs Days (Samples fabricated at a different blend ratio of P3HT:PC_{61}BM with the variation of thickness).

In this work section, all the devices were encapsulated and placed on the laboratory window under ambient and light conditions. Figure 18 demonstrates the stability of all air process OSCs placed in a real-time environment and records the continuous change in maximum voltage with the time interval of 20 min/each day for 30 days. According to Figure 18, at 800 rpm, the behaviour exhibited for each blend system ratio was distinct. In a blended system of 1.0:0.6, the OSCs device displayed a low maximum output voltage until the 5th day and then increased significantly. The maximum voltage recorded was 0.365 mV on the 9th day with a device lifetime of 22 days. As regards to 1.0:0.8 ratio, the device exhibited a constant behaviour with a slight voltage decrease on the 25th day. The maximum voltage value was 0.451 mV on the 2nd day with a device lifetime of 30 days. Finally, in a blended system of 1.0:1.0, the SC device had a uniform behaviour until the 10th, and from this day on, the device performance was unconstant. The maximum recorded value was 0.454 mV and a device lifetime of 30 days.

Concerning 1000 rpm, the device voltage was approximately constant in all the blend system. Both devices with a photoactive blend ratio of 1.0:06 and 1:0.8 had a lifetime of 30 days and at a blend ratio of 1.0:1.0, the device lifetime was 22 days. The maximum recorded value for

1.0:0.6, 1.0:0.8 and 1.0:1.0 ratio was 0.478 mV, 0.458 mV and 0.461 mV, respectively, on the corresponding 1st, 2nd and 1st days.

Regarding 1200 rpm, in a blended system of 1.0:0.6, the device initially exhibited a low output voltage, and on the 20th day, the output voltage raised and had a constant behaviour. The maximum voltage value of 0.443 mV was registered on the 25th. On a blended system of 1.0:0.8, on the 5th, day the maximum voltage decayed and then rose again, remaining constant until the last day. The device exhibited a maximum output voltage and a short lifetime of 0.318 mV and 13 days, respectively. Finally, on a blended system of 1.0:1.0, the voltage values were conforming and homogeneous, without significant oscillations. The maximum voltage value recorded was 0.432 mV on the 22nd day, and the device lifetime was 22 days.

Ultimately, at a spin-speed of 1500 rpm for a blended system of 1.0:0.6, the voltage values were extremely inconsistent (oscillations). The maximum output voltage was 0.464 mV on the 1st day, and the device lifetime was 24 days. As regards to 1.0:0.6 ratio, the device performance behaviour was also inconsistent, and a short device lifetime of 15 days was observed. The maximum voltage value recorded was 0.308 mV. For a blend ratio of 1:1, the device exhibited a uniform behaviour along the 23 days of the measurement, with a maximum voltage value of 0.401 mV registered on the 11th and 12th days.

In conclusion, it was possible to observe disturbances in the power system where the output voltage became unstable and eventually collapsed, which could indicate that the encapsulation, in some cases, was not able to entirely prevent water (humidity) or oxygen from disturbing the device. The devices with a blended system of 1.0:0.8 exhibit a relatively constant output voltage, but insufficient long-term stability. On a blended system of 1.0:1.0 ,the devices exhibited lower voltage values in comparison to 1.0:0.8, but better long-term stability.

Chapter 4: Conclusions and Future Perspectives

As previously mentioned, the main goal of the present dissertation was to comprehend the relationship between the device performance, optical (absorbance and photoluminescence), 3D morphology of air processed photoactive layers of different thickness (800 rpm, 1000 rpm, 1200 rpm and 1500 rpm) and $PC_{61}BM$ concentrations (1.0:0.6; 1.0:0.8 and 1.0:1.0 ratios) in rrP3HT:$PC_{61}BM$ bulk-heterojunction solar cells.

4.1 Conclusion

In the first part of the developed work, an in-depth study of the UV-Vis absorption spectra of pristine rrP3HT and rrP3HT:$PC_{61}BM$ thin films showed a typical behaviour with thickness dependence. The pristine rrP3HT films show a strong absorption between 400-650 nm with two vibronic features at 603 nm, 555 nm, and one absorption peak at 523 nm. The peaks wavelength (λ) remained constant for all the spin-speeds (thicknesses), although the absorption intensity decreased gradually as the spin-speed (rpm) increased, which translated in less film thickness, contributing to less photon absorption. As regards to rrP3HT:$PC_{61}BM$ absorption, three features at 603 nm, 555 nm, 527 nm, attributed to P3HT excitonic absorption, and an absorption shoulder in the wavelength range between 320-350 nm, attributed to fullerene ($PC_{61}BM$) molecules. Furthermore, the optical absorption displayed a reduction in rrP3HT:$PC_{61}BM$ absorption intensities, as the photoactive layer decreased, resulting from high spin-speed rotations. Besides the thickness impact on the optical response, the influence of $PC_{61}BM$ concentration was investigated. The peak 336 nm and the absorption band, 500-625 nm, were notably influenced by the fullerene (acceptor) concentration. The optical response associated to the first cited peak, which is related to the $PC_{61}BM$ contribution, increased with the concentration of PCBM in all the spin-speeds. In relation to the wavelength range bewtween 500 to 625 nm, two different behaviors were observed: 1st when the spin-speed was 800 rpm and 1500 rpm, as the $PC_{61}BM$ concentration increased, the optical response decreased in all the blend ratios; 2nd the absorbance increased with the increase of $PC_{61}BM$ concentration when the applied spin-speed was 1000 rpm and 1200 rpm. Therefore, the quenching is not linear as the $PC_{61}BM$ increases, which could be attributed to different morphology arrangements during the slow growth of the thin film.

On a second stage, the intermolecular charge transfer (CT) dynamics between rrP3HT and $PC_{61}BM$ molecules were investigated via Photoluminescence (PL). For pristine rrP3HT two vibronic peaks were visible at 650 nm and 710 nm, related to the intrachain and interchain radiative recombination of excitons in the polymer molecules, respectively. The photoluminescence response of the system (rrP3HT:$PC_{61}BM$) was quenched by the increase of $PC_{61}BM$ concentration due to the escalation of charge transfer and fewer recombination rates.

The 3D interpenetrating networks of donor and acceptor materials, characteristic of the active layer structure, were investigated by performing AFM on tapping mode. All the pristine rrP3HT and rrP3HT:PC_{61}BM thin films were coated on sITO/ZnO because ZnO was able to reduce substrate roughness, creating a more uniform surface to deposit conjugated polymers. The AFM measurements for rrP3HT showed a homogenous surface in all the spin-speeds. Concerning rrP3HT:$PC6_1$BM, a smooth surface was obtained in all the blend ratio variation at 1200 rpm, which is a vital requirement to achieve a satisfactory device performance. Finally, the resultant photoactive layer thickness was measured via profilometer. As expected, the film thickness increased as the spin-speed decreased, and PC_{61}BM increased.

Thereafter, the proposed OSCs were electrically characterized through *J-V* measurements. The highest PCE achieved was 0.81 %, with a corresponding V_{OC}, J_{SC}, FF, R_S and R_{SH} of 0.47 V, 3.56 $mAcm^{-2}$, 48 %, 33 Ωcm^2 and 476 Ωcm^2, respectively. The presented resistances values are good since, ideally, these two parameters present the values: RS≈0 and $R_{SH}\approx\infty$. However, the low device performance achieved lies in the fact that the glove box was not utilized for device fabrication. Sequentially, the EIS was performed, and one electrical circuit model was successfully designed for all the spin-speeds and PC_{61}BM concentrations, from which R_S, R_{rec1}, R_{rec2}, R_t, CPE_1, CPE_2, τ_1, τ_2, τ_d, τ_n and µ.

Here, the most suitable blend system was 1.0:0.8 with a spin-speed of 1200 rpm. The choice of these parameters guaranteed an optimum optical, morphology and thickness balance, which makes the improvement of the device performance possible.

On the last stage, the long-term stability of the OSCs (previously encapsulated) was investigated up to a maximum of 1 month. It was possible to observe disturbances in the power (V) system, resulting in the collapse of the device. In this study, the best device produced (1.0:0.8 at 1200 rpm) did not show the best long-term stability performance as it was supposed to. The blend system of 1.0:0.6 at 1000 rpm shows the maximum output voltage of 0.478 mV and a lifetime of 30 days. As regards to the other devices lifetime, the encapsulation was not enough to prevent them from the degradation of the mechanism. This way, it is not possible to establish accurately a correlation between the device performance and the long-term stability.

4.1 Future perspectives

To elucidate the driving mechanisms of the resulting morphology in the rrP3HT:PC_{61}BM as the PC_{61}BM content increased, GI-XRD measurements should be carried out. As regards to ZnO (ETL), it would be interesting to produce the NPs using a faster approach, namely, Microwave-assisted synthesis, pushing the commercialization potential. In addition, it would be curious to produce the devices using the commercial and available ITO. As more general future perspectives, it would be interesting to further investigate the degradations mechanisms on OSCs upon encapsulation. For example, combining Dar lock-in thermography (DLIT) and Electroluminescence image (ELI) could give relevant information.

References

[1] O. Ostroverkhova, “Organic Optoelectronic Materials: Mechanisms and Applications,” *Chem. Rev.*, vol. 116, no. 22, pp. 13279–13412, 2016, doi: 10.1021/acs.chemrev.6b00127.

[2] L. Lu, T. Zheng, Q. Wu, A. M. Schneider, D. Zhao, and L. Yu, “Recent Advances in Bulk Heterojunction Polymer Solar Cells,” *Chem. Rev.*, vol. 115, no. 23, pp. 12666–12731, 2015, doi: 10.1021/acs.chemrev.5b00098.

[3] B. O. Esteves, “Perovskite solar cells: Optimization of Cost-Effective Production,” Faculty of Sciences and Technology – New University of Lisbon, 2018.

[4] Y. S. Zimmermann, A. Schäffer, C. Hugi, K. Fent, P. F. X. Corvini, and M. Lenz, “Organic photovoltaics: Potential fate and effects in the environment,” *Environ. Int.*, vol. 49, pp. 128–140, 2012, doi: 10.1016/j.envint.2012.08.015.

[5] C. W. Tang, “Two-layer organic photovoltaic cell,” *Appl. Phys. Lett.*, vol. 48, no. 2, pp. 183–185, 1986, doi: 10.1063/1.96937.

[6] D. Moses, A. Dogariu, and A. J. Heeger, “Ultrafast photoinduced charge generation in conjugated polymers,” *Chem. Phys. Lett.*, vol. 316, no. 5–6, pp. 356–360, 2000, doi: 10.1016/S0009-2614(99)01316-0.

[7] M. Hiramoto and Y. Shinmura, “Organic Solar Cells,” in *Springer Handbook of Electronic and Photonic Materials*, S. Kasap and P. Capper, Eds. Cham: Springer International Publishing, 2017, p. 1.

[8] Q. Liu *et al.*, “18% Efficiency organic solar cells,” *Sci. Bull.*, vol. 65, no. 4, pp. 272–275, 2020, doi: 10.1016/j.scib.2020.01.001.

[9] R. Geethu, C. Sudha Kartha, and K. P. Vijayakumar, “Improving the performance of ITO/ZnO/P3HT: PCBM/Ag solar cells by tuning the surface roughness of sprayed ZnO,” *Sol. Energy*, vol. 120, pp. 65–71, 2015, doi: 10.1016/j.solener.2015.06.037.

[10] R. Geethu, M. V. Santhosh, C. S. Kartha, and K. P. Vijayakumar, “Overcoming consistency constrains of ITO/ZnO/P3HT:PCBM/Ag solar cell by open air annealing and its systematic stability study under inborn conditions,” *J. Mater. Sci. Mater. Electron.*, vol. 30, no. 20, pp. 18981–18989, 2019, doi: 10.1007/s10854-019-02255-3.

[11] M. T. Dang, L. Hirsch, and G. Wantz, “P3HT:PCBM, best seller in polymer photovoltaic research,” *Adv. Mater.*, vol. 23, no. 31, pp. 3597–3602, 2011, doi: 10.1002/adma.201100792.

[12] S. K. Hau, H. L. Yip, and A. K. Y. Jen, “A review on the development of the inverted

polymer solar cell architecture," *Polym. Rev.*, vol. 50, no. 4, pp. 474–510, 2010, doi: 10.1080/15583724.2010.515764.

[13] WEC, "Global Energy Scenarios Comparison Review," *World Energy Insights Brief 2019 - Technical Annex*, p. 35, 2019.

[14] D. R. et al. (Achlatis M. listed as contributing author) Hoegh-Guldberg O., Jacob D., Taylor M., Bindi M., Brown S., Camilloni I., Diedhiou A., "Global warming of 1.5°C. An IPCC Special Report on the impacts of global warming of 1.5°C above pre-industrial levels and related global greenhouse gas emission pathways, in the context of strengthening the global response to the threat of climate change," in *Special Report, Intergovernmental Panel on Climate Change*, no. ISBN 978-92-9169-151-7, Geneva, Switzerland: World Meteorological Organization Technical Document, 2018, pp. 175–311.

[15] H. Y. Hafeez, Z. S. Iro, B. I. Adam, and J. Mohammed, "Fabrication and Characterization of Organic Photovoltaic Cell using Keithley 2400 SMU for efficient solar cell," *J. Phys. Conf. Ser.*, vol. 1000, no. 1, 2018, doi: 10.1088/1742-6596/1000/1/012124.

[16] O. Pachoumi, "Metal Oxide / Organic Interface Investigations for Photovoltaic Devices," *Univ. Cambridge*, no. July, 2014, [Online]. Available: https://doi.org/10.17863/CAM.16614.

[17] W. Wagemans, "Plastic Spintronics: Spin transport and intrinsic magnetoresistance in organic semiconductors," 2010.

[18] V. Jain, B. K. Rajbongshi, A. Tej Mallajosyula, G. Bhattacharjya, S. S. Kumar Iyer, and G. Ramanathan, "Photovoltaic effect in single-layer organic solar cell devices fabricated with two new imidazolin-5-one molecules," *Sol. Energy Mater. Sol. Cells*, vol. 92, no. 9, pp. 1043–1046, 2008, doi: 10.1016/j.solmat.2008.02.039.

[19] T. Xu and Q. Qiao, "Organic Photovoltaics: Basic Concepts and Device Physics," in *Encyclopedia of Nanotechnology*, B. Bhushan, Ed. Dordrecht: Springer Netherlands, 2012, pp. 2022–2031.

[20] M. Rita Narayan and J. Singh, "Study of the mechanism and rate of exciton dissociation at the donor-acceptor interface in bulk-heterojunction organic solar cells," *J. Appl. Phys.*, vol. 114, no. 7, 2013, doi: 10.1063/1.4818813.

[21] Y. Song, K. Zhang, S. Dong, R. Xia, F. Huang, and Y. Cao, "Semitransparent Organic Solar Cells Enabled by a Sequentially Deposited Bilayer Structure," *ACS Appl. Mater. Interfaces*, vol. 12, no. 16, pp. 18473–18481, Apr. 2020, doi: 10.1021/acsami.0c00396.

[22] M. GREEN *et al.*, "Solar cell efficiency tables (version 40)," *Ieee Trans Fuzzy Syst*, vol.

20, no. 6, pp. 1114–1129, 2012, doi: 10.1002/pip.

[23] J. Cirák, "Concept of Organic Photovoltaics: Operational Principles and Materials," *Acta Electrotech. Inform.*, vol. 13, no. 1, 2013, doi: 10.2478/aeei-2013-0006.

[24] H. Gaspar, F. Figueira, L. Pereira, A. Mendes, J. C. Viana, and G. Bernardo, "Recent Developments in the Optimization of the Bulk Heterojunction Morphology of Polymer: Fullerene Solar Cells," *Mater. (Basel, Switzerland)*, vol. 11, no. 12, p. 2560, Dec. 2018, doi: 10.3390/ma11122560.

[25] S. Rafique, S. M. Abdullah, K. Sulaiman, and M. Iwamoto, "Fundamentals of bulk heterojunction organic solar cells: An overview of stability/degradation issues and strategies for improvement," *Renew. Sustain. Energy Rev.*, vol. 84, no. November 2017, pp. 43–53, 2018, doi: 10.1016/j.rser.2017.12.008.

[26] L. Benatto, K. R. de A. Sousa, and M. Koehler, "Driving Force for Exciton Dissociation in Organic Solar Cells: The Influence of Donor and Acceptor Relative Orientation," *J. Phys. Chem. C*, vol. 124, no. 25, pp. 13580–13591, Jun. 2020, doi: 10.1021/acs.jpcc.0c03116.

[27] A. Saeki, "Evaluation-oriented exploration of photo energy conversion systems: from fundamental optoelectronics and material screening to the combination with data science," *Polym. J.*, vol. 52, no. 12, pp. 1307–1321, 2020, doi: 10.1038/s41428-020-00399-2.

[28] J. D. A. Lin *et al.*, "Systematic study of exciton diffusion length in organic semiconductors by six experimental methods," *Mater. Horizons*, vol. 1, no. 2, pp. 280–285, 2014, doi: 10.1039/c3mh00089c.

[29] L. E. De Sousa, F. T. Bueno, G. M. E Silva, D. A. Da Silva Filho, and P. H. D. O. Neto, "Fast predictions of exciton diffusion length in organic materials," *J. Mater. Chem. C*, vol. 7, no. 14, pp. 4066–4071, 2019, doi: 10.1039/c9tc00153k.

[30] M. C. Heiber and A. Dhinojwala, "Dynamic Monte Carlo modeling of exciton dissociation in organic donor-acceptor solar cells," *J. Chem. Phys.*, vol. 137, no. 1, 2012, doi: 10.1063/1.4731698.

[31] S. Ono and K. Ohno, "Origin of Charge Transfer Exciton Dissociation in Organic Solar Cells," *Excitons*, 2018, doi: 10.5772/intechopen.69854.

[32] C. M. Proctor, M. Kuik, and T. Q. Nguyen, "Charge carrier recombination in organic solar cells," *Prog. Polym. Sci.*, vol. 38, no. 12, pp. 1941–1960, 2013, doi: 10.1016/j.progpolymsci.2013.08.008.

[33] T. Shan *et al.*, "Universal and versatile morphology engineering via hot fluorous solvent soaking for organic bulk heterojunction," *Nat. Commun.*, vol. 11, no. 1, 2020, doi:

10.1038/s41467-020-19429-x.

[34] D. Chen, C. Zhang, Z. Wang, R. Gao, and Y. Hao, "Differences of conventional and inverted organic solar cells in optical aspect," *ICSICT 2012 - 2012 IEEE 11th Int. Conf. Solid-State Integr. Circuit Technol. Proc.*, pp. 2–4, 2012, doi: 10.1109/ICSICT.2012.6467744.

[35] F. Zhang *et al.*, "Recent development of the inverted configuration organic solar cells," *Sol. Energy Mater. Sol. Cells*, vol. 95, no. 7, pp. 1785–1799, 2011, doi: 10.1016/j.solmat.2011.02.002.

[36] S. Pitchaiya *et al.*, "A review on the classification of organic/inorganic/carbonaceous hole transporting materials for perovskite solar cell application," *Arab. J. Chem.*, vol. 13, no. 1, pp. 2526–2557, 2020, doi: 10.1016/j.arabjc.2018.06.006.

[37] M. Hilal and J. I. Han, "The effect of the functionalization of multiple carrier transporting interlayers on the performance and stability of bulk heterojunction organic solar cells," *J. Mater. Sci. Mater. Electron.*, vol. 29, no. 16, pp. 13561–13576, 2018, doi: 10.1007/s10854-018-9484-3.

[38] K. Anagnostou, M. M. Stylianakis, and K. Petridis, "Building an Organic Solar Cell : Fundamental," no. c, 2019, doi: https://doi.org/10.3390/en12112188.

[39] Z. Yin, J. Wei, and Q. Zheng, "Interfacial Materials for Organic Solar Cells: Recent Advances and Perspectives," *Adv. Sci.*, vol. 3, no. 8, pp. 1–37, 2016, doi: 10.1002/advs.201500362.

[40] R. Søndergaard, M. Hösel, D. Angmo, T. T. Larsen-Olsen, and F. C. Krebs, "Roll-to-roll fabrication of polymer solar cells," *Mater. Today*, vol. 15, no. 1–2, pp. 36–49, 2012, doi: 10.1016/S1369-7021(12)70019-6.

[41] M. Habibi and M. Eslamian, "Facile and low-cost mechanical techniques for the fabrication of solution-processed polymer and perovskite thin film transistors," *J. Phys. Commun.*, vol. 2, no. 7, 2018, doi: 10.1088/2399-6528/aad3a6.

[42] M. Rizwan and K. Niazi, "Solution Processing of Small Molecule Organic Semiconductors : From In situ Investigation to the Scalable Manufacturing of Field Effect Transistors," 2018, [Online]. Available: http://hdl.handle.net/10754/628035.

[43] H. Hoppe and N. S. Sariciftci, "Organic solar cells: An overview," *J. Mater. Res.*, vol. 19, no. 7, pp. 1924–1945, 2004, doi: 10.1557/JMR.2004.0252.

[44] M. D. Tyona, "A theoritical study on spin coating technique," *Adv. Mater. Res.*, vol. 2, no. 4, pp. 195–208, 2013, doi: 10.12989/amr.2013.2.4.195.

[45] F. C. Krebs, "Fabrication and processing of polymer solar cells: A review of printing and

coating techniques," *Sol. Energy Mater. Sol. Cells*, vol. 93, no. 4, pp. 394–412, 2009, doi: 10.1016/j.solmat.2008.10.004.

[46] W. Nie *et al.*, "Exploring spray-coating techniques for organic solar cell applications," *Int. J. Photoenergy*, vol. 2012, pp. 1–8, 2012, doi: 10.1155/2012/175610.

[47] A. Reale *et al.*, "Spray Coating for Polymer Solar Cells: An Up-to-Date Overview," *Energy Technol.*, vol. 3, no. 4, pp. 385–406, 2015, doi: 10.1002/ente.201402180.

[48] W. Wang, J. Qu, P. S. B. Julião, and Z. Shao, "Cover Feature: Recent Advances in the Development of Anode Materials for Solid Oxide Fuel Cells Utilizing Liquid Oxygenated Hydrocarbon Fuels: A Mini Review (Energy Technol. 1/2019)," *Energy Technol.*, vol. 7, no. 1, pp. 2–2, 2019, doi: 10.1002/ente.201980102.

[49] E. Pérez-Gutiérrez *et al.*, "Organic solar cells all made by blade and slot–die coating techniques," *Sol. Energy*, vol. 146, pp. 79–84, 2017, doi: 10.1016/j.solener.2017.02.004.

[50] J. Yang *et al.*, "Roll-to-Roll Slot-Die-Printed Polymer Solar Cells by Self-Assembly," *ACS Appl. Mater. Interfaces*, vol. 10, no. 26, pp. 22485–22494, Jul. 2018, doi: 10.1021/acsami.8b05673.

[51] L. M. Andersson, "Fully Slot-Die-Coated All-Organic Solar Cells," *Energy Technol.*, vol. 3, no. 4, pp. 437–442, 2015, doi: 10.1002/ente.201402153.

[52] O. Ostroverkhova, "Informatics for Materials Science and Engineering," in *Informatics for Materials Science and Engineering*, vol. 116, no. 22, Butterworth-Heinemann (July 10, 2013), 2013, pp. 13279–13412.

[53] V. Bharti, S. Chand, and V. Dutta, "Realization of Highly Efficient Polymer Solar Cell Based on PBDTTT-EFT and [71] PCBM," vol. 140084, 2018, doi: 10.1063/1.5029215.

[54] M. Picollo, M. Aceto, and T. Vitorino, "UV-Vis spectroscopy," *Phys. Sci. Rev.*, vol. 4, no. 4, pp. 1–14, 2019, doi: 10.1515/psr-2018-0008.

[55] F. C. Chen, "Organic semiconductors," in *Encyclopedia of Modern Optics*, vol. 1–5, A. Boudrioua, M. Chakaroun, and A. B. T.-O. L. Fischer, Eds. Elsevier, 2018, pp. 220–231.

[56] P. J. Worsfold, "UV—visible Spectroscopy and its Applications," *Anal. Chim. Acta*, vol. 284, no. 1, p. 245, 1993, doi: 10.1016/0003-2670(93)80039-n.

[57] T. Mayerhöfer, "The Bouguer-Beer-Lambert Law : Shining Light on the Obscure The Bouguer-Beer-Lambert Law : Shining Light on the Obscure," no. July, 2020, doi: 10.1002/cphc.202000464.

[58] J. Müllerová, M. Kaiser, V. Nádaždy, P. Šiffalovič, and E. Majková, "Optical absorption study of P3HT: PCBM blend photo-oxidation for bulk heterojunction solar cells," *Sol.*

Energy, vol. 134, no. January 2018, pp. 294–301, 2016, doi: 10.1016/j.solener.2016.05.009.

[59] G. Li, V. Shrotriya, Y. Yao, and Y. Yang, "Investigation of annealing effects and film thickness dependence of polymer solar cells based on poly(3-hexylthiophene)," *J. Appl. Phys.*, vol. 98, no. 4, pp. 1–6, 2005, doi: 10.1063/1.2008386.

[60] L. Kerkeni *et al.*, "We are IntechOpen , the world ' s leading publisher of Open Access books Built by scientists , for scientists TOP 1 %," *Intech,* no. tourism, p. 13, 2016, [Online]. Available: https://www.intechopen.com/books/advanced-biometric-technologies/liveness-detection-in-biometrics.

[61] D. Lee, J. Kim, S. Noh, and C. Lee, "The thickness of active layer dependence of polymer solar cells," in *2010 10th IEEE Conference on Nanotechnology, NANO 2010,* 2010, pp. 1175–1178, doi: 10.1109/NANO.2010.5698038.

[62] B. Kadem, A. Hassan, and W. Cranton, "Performance optimization of P3HT:PCBM solar cells by controlling active layer thickness," pp. 1090–1094.

[63] J. W. Kingsley, A. Green, and D. G. Lidzey, "Fabrication and optimization of P3HT:PCBM organic photovoltaic devices," *Org. Photovoltaics X,* vol. 7416, no. October 2014, p. 74160T, 2009, doi: 10.1117/12.829178.

[64] L. Brand and M. L. Johnson, "An Introduction to Fluorescence Spectroscopy," p. 15, 2011, [Online]. Available: http://books.google.com/books?id=GgFXweh0hmQC&pgis=1.

[65] M. J. Sanderson, I. Smith, I. Parker, and M. D. Bootman, "Topic Introduction Fluorescence Microscopy," 2014, doi: 10.1101/pdb.top071795.

[66] M. O. Manasreh, *Introduction to defects and structural properties of Ill-nitride semiconductors*. 2000.

[67] "Photoluminescence Spectroscopy - an overview | ScienceDirect Topics." [Online]. Available: https://www.sciencedirect.com/topics/chemistry/photoluminescence-spectroscopy.

[68] S. H. Chang, C. Chiang, H. Cheng, C. Tai, and C. Wu, "Broadband charge transfer dynamics in P3HT : PCBM blended film," no. December, 2013, doi: 10.1364/OL.38.005342.

[69] J. Bergström, "2 - Experimental Characterization Techniques," J. B. T.-M. of S. P. Bergström, Ed. William Andrew Publishing, 2015, pp. 19–114.

[70] J. R. O'Dea, L. M. Brown, N. Hoepker, J. A. Marohn, and S. Sadewasser, "Scanning probe microscopy of solar cells: From inorganic thin films to organic photovoltaics," *MRS Bull.*, vol. 37, no. 7, pp. 642–650, 2012, doi: 10.1557/mrs.2012.143.

[71] P. Nguyen-Tri, P. Ghassemi, P. Carriere, S. Nanda, A. A. Assadi, and D. D. Nguyen, “Recent applications of advanced atomic force microscopy in polymer science: A review,” *Polymers (Basel).*, vol. 12, no. 5, pp. 1–28, 2020, doi: 10.3390/POLYM12051142.

[72] S. Maghsoudy-Louyeh, M. Kropf, and B. R. Tittmann, “Review of Progress in Atomic Force Microscopy,” *Open Neuroimag. J.*, vol. 12, no. 1, pp. 86–104, 2019, doi: 10.2174/1874440001812010086.

[73] F. Danielli, B. De Sousa, and C. H. Scuracchio, “The Use of Atomic Force Microscopy as an Important Technique to Analyze the Dispersion of Nanometric Fillers and Morphology in Nanocomposites and Polymer Blends Based on Elastomers,” vol. 24, pp. 661–672, 2014.

[74] O. Oklobia, “Investigations of Thermally Induced Morphology in P3HT / PCBM Thin Films : Influence of Composition and Thermal Annealing on Photovoltaic Properties Ochai Oklobia A thesis submitted in partial fulfilment of the requirement of Staffordshire University for,” no. February, 2016.

[75] Q. Wu, M. Bhattacharya, L. M. J. Moore, and S. E. Morgan, “Air Processed P3HT : PCBM Photovoltaic Cells : Morphology Correlation to Annealing , Degradation , and Recovery,” pp. 1–10, 2014, doi: 10.1002/polb.23605.

[76] N. Sharma, S. K. Gupta, C. Mohan, and S. Negi, “Superlattices and Microstructures Influence of active layer thickness on photovoltaic performance of PTB7 : PC70BM bulk heterojunction solar cell,” *Superlattices Microstruct.*, vol. 135, no. September, p. 106278, 2019, doi: 10.1016/j.spmi.2019.106278.

[77] M. Kim, B. Kim, and J. Kim, “Effective Variables To Control the Fill Factor of Organic Photovoltaic Cells,” vol. 1, no. 6, pp. 1–6, 2009, doi: 10.1021/am900155y.

[78] C. M. Proctor and T. Nguyen, “Effect of leakage current and shunt resistance on the light intensity dependence of organic solar cells,” vol. 083301, no. November 2014, 2015, doi: 10.1063/1.4913589.

[79] A. Manuscript, “Materials Chemistry,” no. 207890, 2012, doi: 10.1039/b000000x.

[80] S. Berson, “Solar Energy Materials & Solar Cells Impedance spectrometry of optimized standard and inverted P3HT-PCBM organic solar cells,” vol. 101, pp. 210–216, 2012, doi: 10.1016/j.solmat.2012.01.013.

[81] N. Wagner, “Electrochemical impedance spectroscopy,” *PEM Fuel Cell Diagnostic Tools*, no. 1, pp. 37–70, 2011, doi: 10.1201/b11100-5.

[82] S. P. Ravishankar, “Device Modelling of Perovskite Solar Cells using Small Perturbation Methods,” 2019.

[83] S. Ali, S. Chang, M. Imran, Q. Shi, Y. Chen, and H. Zhong, “Impedance Spectroscopy: A Versatile Technique to Understand Solution-Processed Optoelectronic Devices,” *Physica Status Solidi - Rapid Research Letters*, vol. 13, no. 5. pp. 1–16, 2019, doi: 10.1002/pssr.201800580.

[84] V. Sály, M. Váry, and M. Pern, “Applied Surface Science AC characterization of bulk organic solar cell in the dark and under illumination ˇ,” vol. 312, pp. 176–181, 2014, doi: 10.1016/j.apsusc.2014.06.021.

[85] J. Y. Kim, “Effect of solvents on the electrical and morphological characteristics of polymer solar cells,” *Polymers (Basel).*, vol. 11, no. 2, 2019, doi: 10.3390/polym11020228.

[86] S. Rao, R. Sharma, G. Srinivas, S. Kundu, and D. Gupta, “Incorporation of silver and gold nanostructures for performance improvement in P3HT : PCBM inverted solar cell with rGO / ZnO nanocomposite as an electron transport layer Incorporation of silver and gold nanostructures for performance improvement in P3HT ,” *Org. Electron.*, vol. 29, no. February, pp. 79–87, 2016, doi: 10.1016/j.orgel.2015.11.015.

[87] L. Xu, Y. J. Lee, and J. W. P. Hsu, “Charge collection in bulk heterojunction organic photovoltaic devices: An impedance spectroscopy study,” *Appl. Phys. Lett.*, vol. 105, no. 12, pp. 28–33, 2014, doi: 10.1063/1.4896633.

[88] R. Bachelor and P. Physics, “Equivalent circuit analysis on organic solar cells : how can impedance spectroscopy results be interpreted ? Sofie ten Have Second assessor : Rick Bethlem,” 2017.

[89] S. K. Gupta, L. S. Pali, and A. Garg, “Impedance spectroscopy on degradation analysis of polymer / fullerene solar cells,” *Sol. Energy*, vol. 178, no. December 2018, pp. 133–141, 2019, doi: 10.1016/j.solener.2018.12.024.

[90] R. N. Chauhan, C. Singh, R. S. Anand, and J. Kumar, “Effect of Sheet Resistance and Morphology of ITO Thin Films on Polymer Solar Cell Characteristics,” vol. 2012, 2012, doi: 10.1155/2012/879261.

[91] S. B. Sapkota and S. Hi-tech, “Long-term stability of organic solar cells,” no. November, 2019.

[92] E. çetin Yilmaz, M. K. Yeşilyurt, I. V. öner, G. ömeroğlu, and A. N. özakin, “Operational stability and degradation of organic solar cells,” *Period. Eng. Nat. Sci.*, vol. 5, no. 2, pp. 152–160, 2017, doi: 10.21533/pen.v5i2.105.

APPENDIX: A

A.1 Materials:

Table A.1 lists the materials used in the proposed research work. All the materials are utilized without any further purification.

Table A.1 | List of reagents used throughout this work with respective abbreviation, purity, CAS and company.

Materials	Formula / Synonym	Purity (%)	Companies
Zinc Acetate dihydrate	$Zn(OAc)_2$		Sigma- Aldrich
Potassium hydroxide	KOH		EKA
Molybdenum (VI) oxide	MoO_3		Sigma- Aldrich
Regioregular poly(3-hexylthiophene-2,5-diyl)	rrP3HT		Ossila
[6,6]-Phenyl-C61 butyric acid methyl ester	$PC_{61}BM$		Sigma- Aldrich
Sodium bicarbonate	$NaHCO_3$		LabChem Inc.
Hydrochloric acid	HCL		Honeywell
Hydrogen peroxide	H_2O_2		LabChem Inc.
Chloroform	$CHCL_3$		Sigma- Aldrich
1,2-Dichlorobenzene	o-DCB	99	Sigma- Aldrich
Acetone	CH_3COCH_3		LabChem Inc.
Isopropyl alcohol	IPA		LabChem Inc.
Ethanol	CH_3CH_2OH		LabChem Inc.
Methanol	CH_3OH / MeOH		Sigma- Aldrich
E131 Encapsulation Epoxy	-NA-		Ossila
Evaporation Material Silver pallets	Ag pallets	99.999	Alpha Aesar
Evaporation Boat (Molybdenum)			Kurt J. Lesker

A.2 Procedure for the synthesis of ZnO nanoparticles:

The ZnO nanoparticles were synthesized by the hydroxylation of $Zn(OAc)_2$ with KOH in the presence of MeOH solvent at the temperature of 62ºC for 2.5-3 Hr. For the synthesis, 2.95 gm of $Zn(OAc)_2$ were mixed in 125 ml of methanol in a constant stirring at 62ºC. the other solution of 1.48 gm of KOH in 65 ml of MeOH was prepared. When $Zn(OAc)_2$ dissolved completely, the KOH solution was added to it. After adding the KOH solution, the reaction mixture was left stirring for 2.5-3 hr at a constant temperature of 62ºC. When the reaction completed, the solution was removed from temperature and kept overnight for precipitation. Next day, the solvent was removed, the NPs washed 2-3 times, with methanol solvent. After washing, the ZnO NPs was dissolved in the mixture of chloroform and 1-butanol solvent. Before the application of ZnO nanoparticles, it was filtered with 0.45 µm PTFE filter. Figure A.1 shows the schematic overview of the synthesis and collected ZnO nanoparticle under UV light.

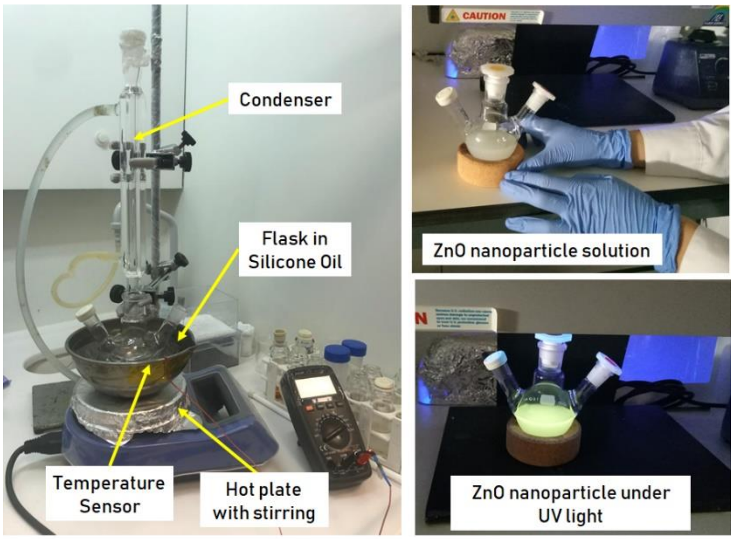

Figure A1 | Schematic overview of the synthesis of ZnO nanoparticle and ZnO nanoparticles under UV light.

A.3 AFM Measurements:

Figure A2 shows the 3D topography image of sputtered sITO and ZnO nanoparticle film on the sITO substrate. From the 3D view, it is observed that the deposition of ZnO nanoparticles significantly improves the surface morphology of the sITO. The ZnO nanoparticle files show the homogenous morphology all over.

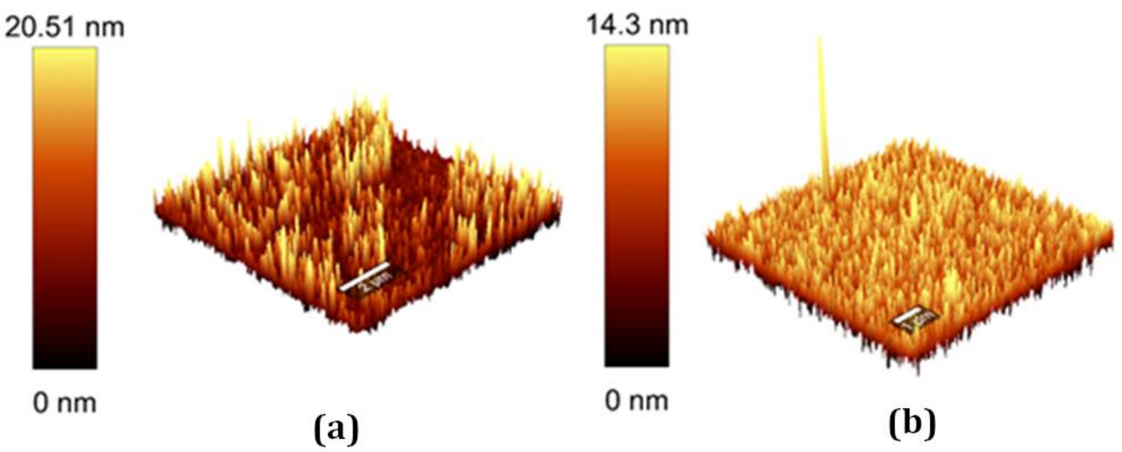

Figure A2 | 3D view of the AFM topography image of (a) sITO (b) ZnO nanoparticles deposited on sITO substrate.

The 3D view of the AFM topography image of pristine P3HT at the various thickness and blend of P3HT:$PC_{61}BM$ and at the different thickness and $PC_{61}BM$ concentration are shown in Figure A3, A4 respectively.

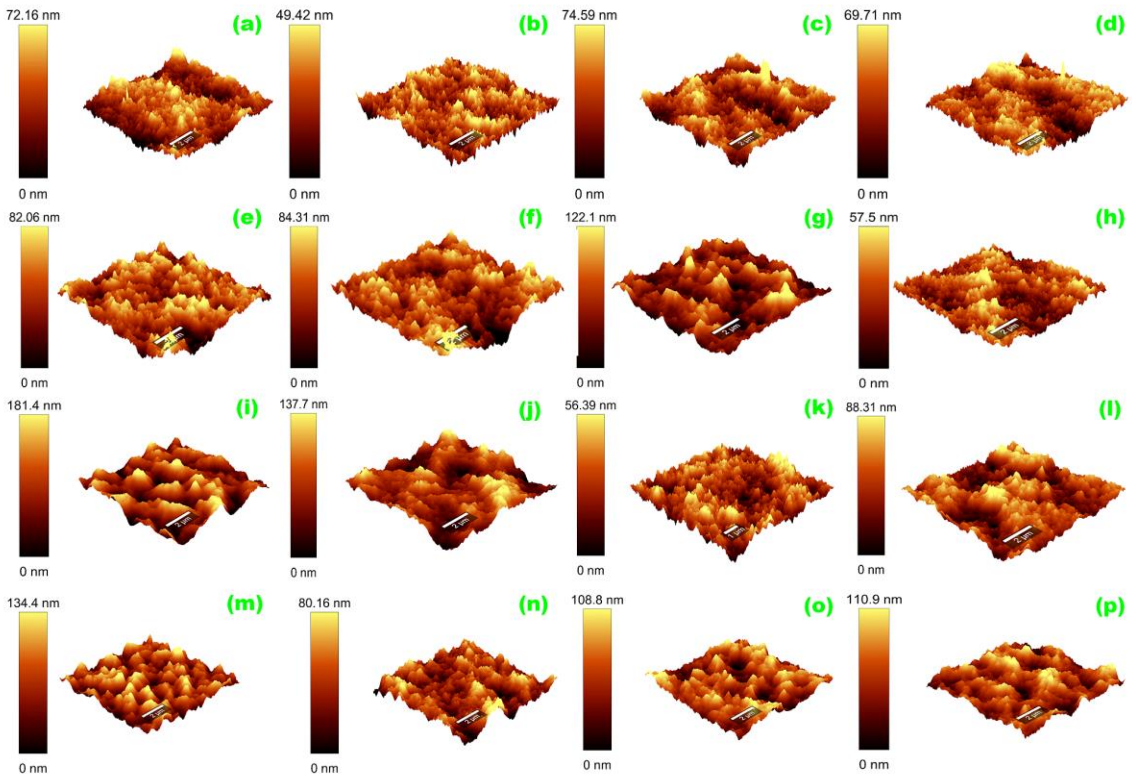

Figure A3 | 3D view of the AFM topography image of pristine rrP3HT film, P3HT:PC61BM blend at 1.0:0.6, 1:0.8 and 1.0:1.0 (a) 800 rpm, (b) 1000 rpm, (c) 1200 rpm and (d) 1500 rpm.

A.4 *J-V* characteristics under dark conditions

This section presents the *J-V* characteristics of OSCs devices under dark with the variation of active layer thickness and $PC_{61}BM$ concentration in the blend ratio.

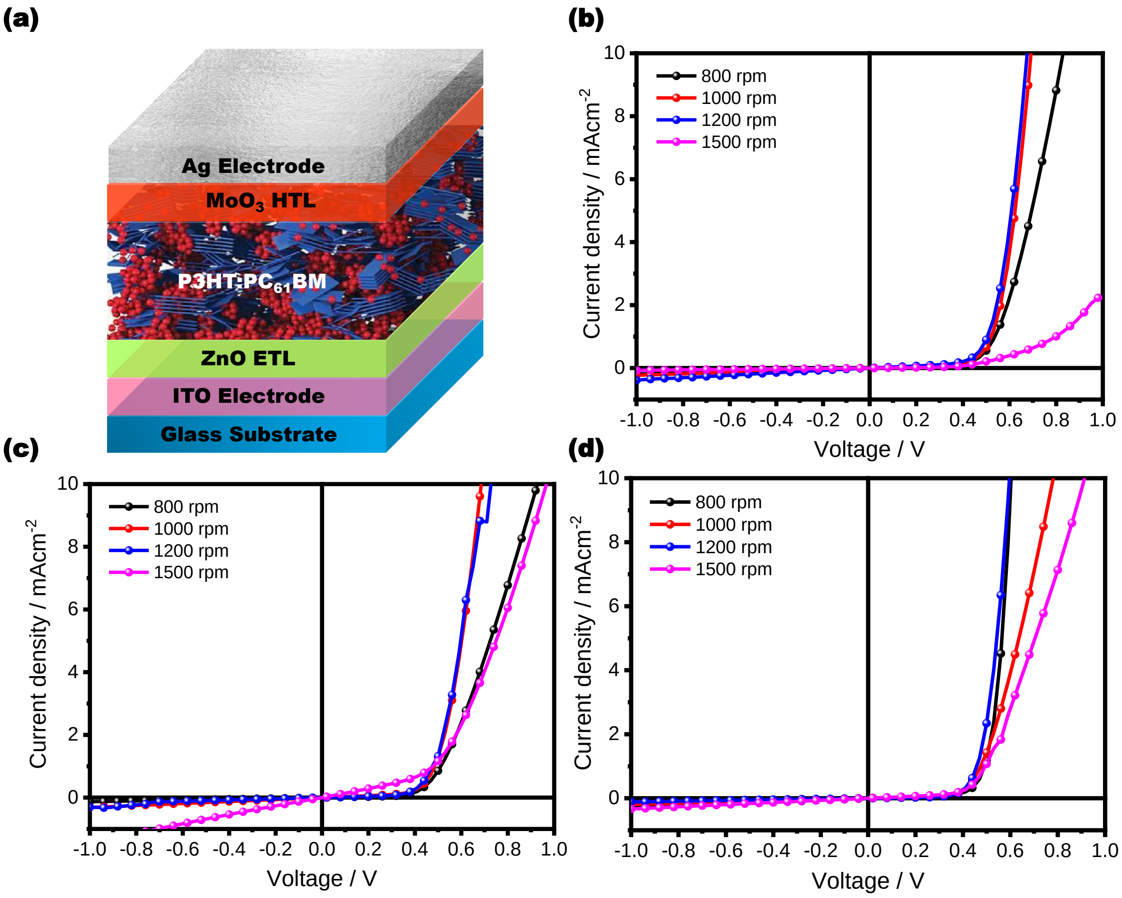

Figure A4 | Device structure (a) and *J-V* characteristics of proposed devices at different blend ratio of (b) 1:0.6, (c) 1:0.8 and (d) 1:1. In all the systems, the photoactive layer was coated at a speed-spin of 800 rpm (black), 1000 rpm (red), 1200 rpm (blue) and 1500 rpm (pink) under dark condition.

A.5 Method to extract photovoltaic performance parameters calculation:

In this section, the calculations of the solar cells parameters are explained through *I-V* curves. The electrical characterization of the photovoltaic cells was carried out by using a low-precision Solar Simulator from the Center's Nanotechnology laboratory Materials Research, at the Materials Science Department, as demonstrated in Figure A5. For the *J-V* measurements, it is necessary to understand how to calculate the photovoltaic parameters. Following there is a detailed description of the calculations.

After the fabrication of OSCs, it was essential to know how efficiently the devices converted the incident light into electricity. For this purpose, the maximum power (P_{max}) was calculated using the following equation:[51]

$$P_{\max} = I_{mp} \times V_{mp}$$

where I_{mp} and V_{mp} are the current and voltage at which the P_{max} occurs. Sequentially, the fill factor (FF), which graphically approximated the area of the largest square from *I-V* characteristics was calculated by [51]:

$$FF = \frac{I_{mp} \times V_{mp}}{I_{SC} \times V_{OC}}$$

Where I_{SC} is the short-circuit current and V_{OC} is the open-circuit voltage. Finally, the power conversion efficiency (PCE) is given by Equation (3) below and it is representative of the overall functionality of a solar cell.[51]

$$PCE = \frac{P_{out}}{P_{in}} \times 100\%$$

Where P_{in} is the incident light power, in this specific case, 1000 W/m^2. Figure A5 illustrates *I-V* curves for the calculation of series resistance (R_S) and shunt resistance (R_{SH}). The R_S and R_{SH} were obtained by the inverse of the slope of *I-V* curves. Ideally, these two parameters present the values: R_S, that should be near to zero, and $R_{SH,}$ near to infinity. Figure A.7 displays the influence of both resistances in the *I-V* characteristics. Finally, Figure A.5 shows the influence of these two resistances in the *I-V* curves and FF.

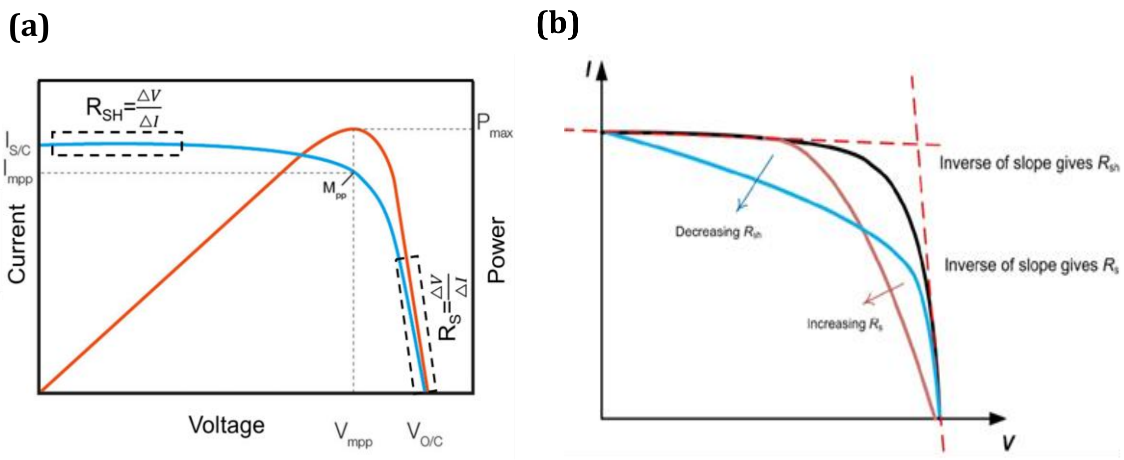

Figure A5 | (a) Illustration of *I-V* and *P-V* curves for calculation of solar cell parameters (b) Influence of series (red) and shunt (blue) resistance (R_S and R_{SH}) in the solar cell I-V curve. Improving series resistance and decreasing shunt resistance may induce the reduction of Isc and Voc, respectively. Adapted from [71]

A.6 Thickness Measurement of Active Layer:

Surface profilers technique has been broadly accepted as an approved solution for measuring the thickness of the thin film. A profilometer uses a stylus (tip), which is scanned vertically and laterally in contact mode with the film for a specified range. It accurately measures small changes in stylus displacement as a function of position. The thickness of the photoactive layer is a significant parameter for OSCs, and actively influences the device performance. Before the thickness measurement, stylus surface profilometer requires a scratch in the active layer and then the sample is placed under the stylus. The thickness of the layer is estimated by measuring the step height (formed by scratch) between the film (R point) and substrate (M point) as shown in Figure A6.

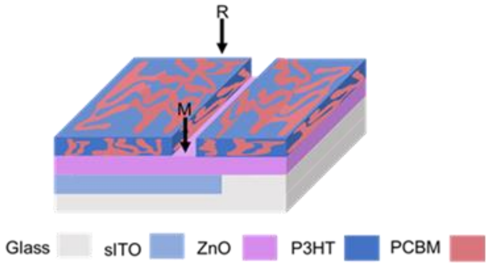

Figure A6 | Schematic diagram of thickness Measurement by using the surface stylus profilometer

Table A.2 | Thickness values of P3HT:PC$_{61}$BM thin films (ratio vs. rpm).

Blend ratio	**800 rpm**	**1000 rpm**	**1200 rpm**	**1500 rpm**
1.0:0.6	287 nm	205 nm	185 nm	159 nm
1.0:0.8	295 nm	232 nm	217 nm	194 nm
1.0:1.0	315 nm	260 nm	246 nm	217 nm

A.7 Instruments Used during the Research Work:

Figure A7 | Images of the instruments used in this research work (a) RF Sputtering from MANTIS system (b) UV-ozone cleaner from Ossila (c) Digital spin coater from Ni-Lo Scientific (d) Atomic Force Microscopy step up (ALPHA RAS 300) from WTec (e) UV-VIS-NIR Spectrophotometer JASCO V-770 (f) Thermal Evaporator System from (g) Self-designed solar simulator with halogen Lamp (h) Voltage source meter from Keithley (i) Surface stylus profilometer (ALPHA D-600 Stylus) from KLA Tencor (j) Impedance measurement setup include a light source (Reference 3000™ potentiostat/galvanostat from Gamry)